Photonic crystal light trapping: Beyond 30% conversion efficiency for silicon photovoltaics

Sayak Bhattacharya (iD), and Sajeev John

View Online   Export Citation   CrossMark

Photonic crystal light trapping: Beyond 30% conversion efficiency for silicon photovoltaics

View Online   Export Citation   CrossMark

Sayak Bhattacharya[1,a] (iD) and Sajeev John[2,b]

AFFILIATIONS

[1] Department of Electronics and Communication Engineering, Indraprastha Institute of Information Technology,
New Delhi 110020, India
[2] Department of Physics, University of Toronto, 60 St. George Street, Toronto, Ontario M5S 1A7, Canada

[a] Author to whom correspondence should be addressed: sayak@iiitd.ac.in
[b] john@physics.utoronto.ca

ABSTRACT

The power conversion efficiency of single-junction silicon solar cells has increased only by 1.5% despite extensive efforts over the past two decades. The current world-record efficiencies of silicon solar cells, within the 25%–26.7% range, fall well below the thermodynamic limit of 32.3%. We review the recent progress in photonic crystal light-trapping architectures poised to achieve 28%–31% conversion efficiency in flexible 3–20 μm-thick, single-junction crystalline-silicon solar cells. These photonic crystals utilize wave-interference based light-trapping, enabling solar absorption well beyond the Lambertian limit in the 300–1200 nm wavelength range. Using experimentally feasible doping profiles, carrier lifetimes, surface recombination velocities, and established Auger recombination losses, we review considerations leading to the prediction of 31% efficiency in a 15 μm-thick silicon photonic crystal cell with interdigitated back-contacts. This is beyond the conversion efficiency of any single-material photovoltaic device of any thickness.

I. INTRODUCTION

Sunlight striking the earth provides approximately 173 000 TW of continuous power, roughly 10 000 times more than all worldwide power consumption. The realization of high-efficiency, low-cost, light-weight, flexible, solar energy conversion materials is central to exploiting this limitless but largely untapped resource. Silicon is valuable due to its non-toxicity, abundance, and mature fabrication technology. However, a thin silicon slab is a relatively weak absorber of sunlight due to its indirect electronic bandgap. In order to improve light-capture, a silicon solar cell typically utilizes a textured top surface. Most of the conventional cell designs, with efficiencies higher than 24%,[1–3,6] employ textures that consider light as rays rather than waves. The current world-record, single-junction silicon solar cell with 165 μm thickness has a power conversion efficiency of 26.7%.[6,7] However, this falls well below the thermodynamic efficiency limit of 32.33% for a single-junction crystalline silicon (c–Si) cell at room temperature, under 1-sun illumination.[8] Practical considerations such as Auger recombination and defect-mediated

charge carrier recombination in the bulk and surface of the cell, imperfect trapping of sunlight in the cell, and bandgap narrowing (BGN) of silicon invariably reduce the maximum attainable efficiency to below the thermodynamic limit. Based on the assumption that light is a ray, devoid of all wave-interference effects, a limiting efficiency based solely on Auger charge carrier recombination was proposed.[9] In this oversimplified ray-optics picture, assuming a Lambertian light-trapping limit, a maximum power conversion efficiency of 29.43% was suggested. As a solar cell is made thicker, it absorbs more light but at the same time suffers from increased bulk-recombination. These two competing effects result in an optimum thickness of the cell. Lambertian ray-optics light-trapping[10] and an improved Auger recombination model[11] suggest an optimum thickness of 110 μm for an undoped, hypothetical cell with no other forms of non-radiative charge carrier recombination.[9] For cells that absorb sunlight below the Lambertian limit, the optimum thickness may be considerably greater and the maximum theoretical efficiency considerably less. Following this model, conventional solar cells are typically made hundreds of micrometer thick.

For example, the 25% efficient passivated emitter rear locally diffused (PERL) cell, the polycrystalline silicon on oxide (POLO) cell with 26.1% efficiency, and the current world-record holding Kaneka cell with 26.7% efficiency are 400 μm, 300 μm, and 165 μm thick, respectively.[2,4–6] Ray-optics based conventional cell designs not only portend a limiting efficiency below 29.43% but also involve considerable cost of the cell due to the requirement of high quality, thick c–Si.

An alternative to thick, inflexible, silicon solar cells is thin-film photovoltaics (TFPV). Typically, the light-absorbing layers of TFPV based cells are less than 10 μm thick and consist of direct bandgap materials such as cadmium telluride (CdTe), copper indium gallium diselenide (CIGS), gallium arsenide (GaAs), or perovskites. Among these technologies, GaAs cells are most efficient and have reached a conversion efficiency of 29.1% on a single-junction (world-record held by Alta Devices).[7] However, GaAs is very expensive due to the scarcity of Ga and the toxicity of As is undesirable. To date, the most efficient CIGS and CdTe cells have 22.9% (by Solar Frontier)[12] and 21% (by First Solar)[7] conversion efficiencies, respectively. Not only are the best CdTe and CIGS cells less efficient than the best silicon solar cells, but also the toxicity of Cd, scarcity and environmental concerns associated with Te, scarcity of Ga, slow and non-economical production process of CIGS pose major challenges to the respective TFPV technologies.[13–15] Among the emergent photovoltaic technologies, perovskite or organo-lead halide cells have shown rapid efficiency growth in recent years.[16–18] Recently, 25.2% power conversion efficiency has been achieved in a thin-film perovskite cell.[18] The Shockley–Queisser limit for single-junction perovskite solar cells is approximately 31%, slightly less than that of silicon cells. Multi-junction cell architectures such as perovskite-silicon tandem have the potential to achieve higher efficiency. At present, Oxford PV holds the world-record efficiency of 28% for a perovskite-silicon tandem cell.[18] However, the lack of long-term stability and environmental safety concerns associated with lead (Pb) may outweigh the advantages of perovskite cells. This review focuses on combining the efficient light-trapping capability of photonic crystals (PhC)[19,20] with the non-toxicity, abundance, and well-developed fabrication techniques of Si to develop a cell technology that encompasses the advantages of the existing TFPV and paves the way toward and beyond 30% power conversion efficiency, a far-reaching goal of the photovoltaic industry.

PhC front-side filters have been used to improve performances of thermo-photovoltaic (TPV) cells[21–27] and photodetectors.[28,29] However, the photodiode materials in such applications usually have direct bandgaps. In contrast, our review focuses on unprecedented solar absorption in thin flexible, indirect bandgap silicon-PhCs, rivaling the absorption of much thicker conventional silicon solar cells and other direct bandgap materials. Although PhCs have been used to improve solar absorption in perovskite cells,[30,31] these cells have considerably lower photo-currents in comparison with the silicon-PhCs. Moreover, stability issues associated with the perovskites render these designs less desirable for large-scale practical deployment.

The most challenging task is to design thin-silicon PhCs that absorb sunlight beyond the Lambertian limit. Lambertian light-trapping does not consider the wave nature of light. The derivation of this limit involves a series of assumptions. The Lambertian model involves a hypothetical randomly rough top surface of the

cell, exhibiting no specular reflection of the incident sunlight at any wavelength. In reality, no surface can satisfy this assumption. A second assumption is that rays within the cell are deflected according to the $\cos\theta$ probability distribution function, where θ is the angle relative to the normal. In contrast, wave-interference based light-trapping in photonic crystals, obtained by solving Maxwell's equations, gives rise to intricate energy flow patterns[32,33] such as parallel-to-interface refraction (PIR) of light and vortex-like energy flow. In the case of PIR, the incoming light is refracted along directions almost parallel to the top surface of the cell in contradistinction to the $\cos\theta$ distribution of Lambertian ray-optics.[32] Furthermore, wave-interference gives rise to vortex-like energy flow patterns and slow-light modes inside a photonic crystal that cannot be described by ray-optics.[33] These interference effects lead to very long photon dwell-time in the active layer of the cell and appear as sharp resonant peaks in the absorption spectra of the cell. In contrast to a conventional, Lambertian cell that weakly absorbs sunlight in the 800–1100 nm wavelength range, a much thinner silicon PhC with wave-interference based resonances can absorb significantly more solar energy in this wavelength range. The strategy toward achieving above 30% power conversion efficiency in a silicon solar cell involves (i) light-trapping optimization in thin-silicon PhCs to achieve solar energy absorption exceeding the Lambertian limit, (ii) use of these optimized thin-silicon PhCs (much thinner than the diffusion lengths of the charge carriers) in order to collect more optically generated electron–hole pairs before they recombine, and (iii) optimization of the contact geometries and doping profiles of the cell to reduce the charge carrier recombination further.

We begin with a brief survey of the ray-optics-based Lambertian limit and high-efficiency conventional solar cells in Sec. II. We critically review the underlying assumptions and statistical arguments that lead to the $4n^2$ optical path-length enhancement where n is the real part of the frequency-dependent refractive index of the light-absorbing material. Richter *et al.*[9] considered an ideal Lambertian cell free from both defect-mediated Shockley–Read–Hall (SRH) and surface recombinations. We revisit the Lambertian cell with more realistic finite SRH lifetime and surface recombination velocities (SRVs). In Sec. III, we review the progress made toward light-trapping and solar energy harvesting in photonic crystals. We compare the light-trapping performances of a wide variety of PhC architectures with unit cells consisting of nano-wires,[34–41] conical-pores,[33,42] inverted pyramids,[43–46] and parabolic-pores.[48,49] From this comparison, we discuss why the 10–15 μm-thick inverted pyramid PhC designs provide the best experimentally feasible route to solar energy absorption well beyond the Lambertian limit and silicon solar cells with conversion efficiency in the 28%–31% range.

Wave-interference-based light-trapping leads to very long dwell-times for long-wavelength photons inside the PhC thin-film and increases the probability that trapped photons get absorbed despite the indirect bandgap of silicon. We also consider electronic bandgap narrowing (BGN)[50] and phonon-assisted sub-bandgap energy absorption in c–Si.[51–54] Depending on the injected carrier density and doping concentration, BGN slightly reduces the open-circuit voltage of the cell. Ray-optics based light-trapping in a conventional cell provides negligible solar energy absorption beyond 1100 nm wavelength. Consequently, BGN reduces the efficiency of a

conventional cell. In contrast, the PhC based cells exhibit multiple resonances due to PIR and vortex-like energy flow in the 1100–1200 nm wavelength range. Such resonances allow sufficient sub-bandgap energy absorption to more than compensate the loss of open-circuit voltage due to BGN.[46,47] In Sec. V, we consider the electronic performance of various cell designs and discuss carrier transport optimization strategies to maximize the collection of optically generated charge carriers in thin-film PhC cells. In contrast to the 110 μm optimum thickness of the hypothetical Lambertian cell, the optimum thickness of the silicon PhC cell with Auger recombination[11] and experimentally achievable carrier lifetime falls between 10 and 15 μm. This suggests that thin-film silicon photovoltaics has the potential to leap ahead of competing technologies and surpass the efficiency of any single-junction solar cell made of a single active material.

II. LAMBERTIAN LIGHT-TRAPPING AND EFFICIENCY LIMITS OF CONVENTIONAL SOLAR CELLS

The light-trapping capability of conventional solar cells typically falls below the ray-optics-based Lambertian limit. Ray-optics computations describe light absorption in conventional cells because the relevant feature sizes of these cells are very large as compared to the 300–1200 nm wavelength scales. For such large light-trapping geometries, ray-optics and statistical arguments suggest a putative upper bound of solar absorption. In a more realistic wave-optics picture, this is in fact only a benchmark rather than a true upper bound. To understand this Lambertian benchmark, we consider a slab of thickness L and refractive index n, with a randomly rough surface at the top and a perfectly reflecting mirror (or a perfect conductor) at the bottom (shown in Fig. 1). As the light rays enter the slab from air, they bounce back and forth multiple times between the top and bottom surfaces before escaping the slab. These multiple reflections enhance the effective light-path (L_{trap}) inside the slab. The derivation of L_{trap} is based on three crucial assumptions:

1. The top surface does not cause any specular reflection to the incoming light rays.
2. If a ray inside the slab is incident on the rough surface at an angle less than the critical angle θ_c (where $\sin \theta_c = \frac{1}{n}$) with respect to the surface normal, the surface allows perfect escape of the ray and causes total internal reflection otherwise. Thus,
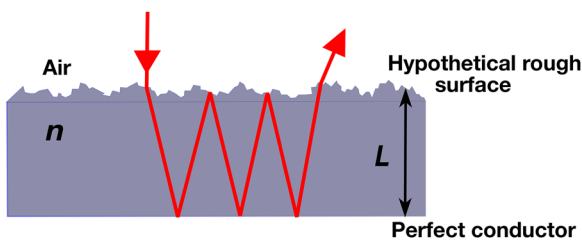

FIG. 1. Geometry used to model statistical ray-trapping in a slab with thickness L and refractive index n, placed on a perfect reflector. The randomly rough top surface is assumed to perfectly transmit all incoming rays into the slab and assumed to provide perfect total internal reflection for rays within the slab incident at an angle greater than the critical angle.

the rays incident within a cone of angle θ_c with respect to the surface normal are able to escape the slab.
3. The top surface randomly redirects both the externally incident rays and total internally reflected rays within the slab at an angle θ with respect to the surface normal, according to a distribution function $f(\theta)$.

According to assumptions 2 and 3, the probability p that the light escapes the slab is given by

$$p = \int_0^{2\pi} d\phi \int_0^{\theta_c} \sin \theta f(\theta) d\theta. \tag{1}$$

For a Lambertian surface, $f(\theta) = \frac{1}{\pi} \cos \theta$, $0 \leq \theta \leq \frac{\pi}{2}$.[55] With this Lambertian distribution of the light rays, Eq. (1) yields $p = 1/n^2$. We define q to be the number of times a ray traverses the distance $2L$ and $G(q)$ to be the probability that the ray escapes after the qth traversal. Thus, $G(1) = p$ and $G(q) = p(1 - p)^{q-1}$ [since the ray does not escape during the first $(q - 1)$ traversal and escapes after the last traversal]. The average number of traversal can be calculated as $\langle q \rangle = \sum_\infty^{q=1} q G(q) = n^2$. When a ray is reflected back to the slab at an angle θ, the path-length of the ray within the slab in each traversal is given by $2L/\cos \theta$. Thus, the average path-length of the rays in a single traversal is given by

$$L_{avg} = \int_0^{2\pi} d\phi \int_0^{\theta_c} \sin \theta f(\theta) \frac{2L}{\cos \theta} d\theta. \tag{2}$$

For a Lambertian surface, the above integral yields $L_{avg} = 4L$. Thus, L_{trap} can be evaluated from the average path-length in $\langle q \rangle$ traversals as $L_{trap} = \langle q \rangle L_{avg} = 4n^2 L$. Alternatively, we can say that the rate of escape of light trapped in the cell is $\frac{v}{L_{trap}}$, where v is the speed of light in the medium. In the literature, this statistical ray-trapping result is widely known as the $4n^2$ limit or the Lambertian limit. The absorption coefficient ($A_{Lambertian}$) of a slab of thickness L and complex refractive index ($n_r - i\kappa$) can then be calculated as a ratio of the rate of absorption to the combined rate of absorption and escape,[10,33]

$$A_{Lambertian} = \frac{\alpha}{L_{trap}^{-1} + \alpha}. \tag{3}$$

Here, α is the wavelength (λ) dependent intrinsic inverse absorption length of the slab material, given by $\alpha = 4\pi\kappa/\lambda$.

Richter et al.[9] modeled maximum light absorption of a silicon solar cell using Eq. (3) and calculated the 29.43% efficiency limit and optimum cell-thickness of 110 μm at 25 °C for a single-junction cell using a revised model of Auger recombination.[11] However, this estimation ignores all SRH recombination and surface recombination. Moreover, it considers Auger recombination for the case of undoped silicon. In order to compare with the performance of the hypothetical Lambertian cell with a realistic cell, we present a revised version of the Lambertian efficiency limit in Sec. V by taking into account realistic SRH lifetime (τ_{SRH}), surface recombination velocity (SRV), and an appropriate doping profile.

Conventional light-trapping designs of the high-efficiency solar cells rely on ray-optics. Accordingly, the 29.43% limit applies well to cells that satisfy the underlying assumptions. For example, the loss

analysis of the 26.7% Kaneka cell shows that with perfect Lambertian light absorption, no extrinsic recombination (SRH and surface recombination), and no resistive losses, it would reach a conversion efficiency of 29.1%. This is precisely the efficiency limit of a hypothetical Lambertian cell with a p-type substrate having the same thickness (165 μm) and resistivity (3Ω cm) as the Kaneka cell.[6]

Two of the commonly employed ray-trapping architectures in high-efficiency silicon solar cells are pyramids and inverted pyramids. Pyramidal textures on c–Si can be fabricated very easily using wet-etching of silicon with KOH. However, in conventional ray-trapping, these pyramids have length scales much larger than the wavelength of light.[1,2,56–61] For such cells, the pyramid sizes and their arrangements can either be uniform[2] or random.[58,62] Light absorption in solar cells, textured with regular or random arrays of upright pyramids with 10 μm or larger base-lengths, falls below the Lambertian limit even when the silicon thickness approaches 400 μm.[56,57] Ray-trapping in 180 μm-thick solar cell textured with random arrays of inverted and upright pyramids with ~15 μm base-length yields a photo-current density of 36 mA/cm^2. Light absorption in such cells can be modeled accurately using ray-optics based computations.[63–65] However, these thicker cells are inflexible. The high non-radiative bulk-recombination of charge carriers is a major roadblock toward achieving higher efficiency in such cells.

Another popular ray-trapping architecture for photovoltaic applications is a random arrangement of silicon nano-pillars[66] with random cross sections, also known as black silicon.[67–69] So far, the power conversion efficiencies of some of the best black silicon cells are 22.1% and 23.5%,[70,71] still well below the putative efficiency limit of 29.43%.

III. WAVE-INTERFERENCE BASED LIGHT-TRAPPING IN PHOTONIC CRYSTALS

The lattice constants of PhCs are comparable to the wavelength of light. In thin-film PhC solar cells, the overall thickness of the structure is only a small number of wavelengths. In this situation, modeling of light-waves by rays would result in an inaccurate description of energy propagation. Instead, an accurate numerical solution of Maxwell's equations is needed in order to accurately capture the light-trapping effects. Light-trapping in PhCs was originally associated with the complete localization of light within a structure through suppression of electromagnetic density of states in the form of a photonic bandgap.[19,72] In contrast, efficient absorption of broadband light, from an external source, arises from the ability to enhance the electromagnetic density of states in a specific frequency regime of PhCs.[32] The design and fabrication of thin-film PhC nanostructures for photovoltaic applications have been very actively pursued using nano-wire,[34–41,73–81] nano-cone,[33,42,75] and nano-pyramid architectures.[43–45,82] Other complex-shaped unit cells such as roof-mosaic, rose, and zigzag with lattice-periodicity in 920–1000 nm range has also been considered for 20 μm-thick c–Si.[82] Light-trapping approaches, combining PhC and plasmonic resonances, have also been proposed.[83–85] However, parasitic absorption of light in the metal particles and recombination losses at the unpassivated metal–semiconductor interfaces reduce the power conversion efficiency of such cells.

The amount of light absorption in a solar cell is quantified by the maximum achievable photo-current density (MAPD). Under $AM1.5G$ illumination, the MAPD of a cell is given by

$$J_{MAPD} = \int_{\lambda=300nm}^{\lambda_{max}} \frac{e\lambda}{hc}I(\lambda)A(\lambda)d\lambda. \qquad (4)$$

Here, $I(\lambda)$ is the intensity of the $AM1.5G$ spectrum; $A(\lambda)$ is the wavelength dependent absorption of the particular structure; λ_{max} is the maximum wavelength of light that the cell can absorb; and e, h, and c are the electronic charge, Planck's constant, and speed of light, respectively. It is assumed that each absorbed photon creates a single electron–hole pair. In the absence of bulk and surface recombination losses, J_{MAPD} is equivalent to the short-circuit current (J_{SC}) of the solar cell. In the absence of BGN, $\lambda_{max} = 1100$ nm for silicon cells. However, with the inclusion of BGN and phonon-assisted absorption in the Urbach tail,[51–54] λ_{max} is chosen to be 1200 nm.

In order to surpass the 30% efficiency barrier, it is necessary to optimize the light-trapping in a thin-film PhC such that its solar absorption exceeds the Lambertian limit and rivals that of a conventional cell 20 times thicker. A key strategy to achieve this goal is to harness the capability of a thin-film PhC to absorb substantial sunlight beyond 800 nm wavelength, a regime where conventional cells are very weak absorbers of solar energy. Early studies focused on ultra-thin silicon structures with an equivalent bulk thickness on the order of 1 μm. Some of these studies considered structures that are not easily fabricated but through which design principles and physical phenomena could easily be established. Using the finite difference time domain (FDTD)[86] method to solve Maxwell's equations,[87] it was shown that modulated silicon nanowires, arranged in a square lattice and embedded in a SiO$_2$ background, yield a MAPD of 27.7 mA/cm^2, over the 350–1000 nm range, using only 1 μm equivalent c–Si thickness.[40,41] While this PhC is able to absorb 63.7% of the incident solar energy using just 1 μm equivalent silicon-thickness, the MAPD still falls below the Lambertian absorption limit. These nanowires have a significant surface area. Using a modest surface recombination velocity of 100 cm/s at the Si–SiO$_2$ interfaces surrounding each nanowire and a relatively poor recombination velocity of 10^5 cm/s at the bottom metallic contact, a power conversion efficiency of 15% was predicted.[41] While this is far below high-efficiency solar cells, it is noteworthy that with only 1 μm of silicon and suitable geometrical structure, wave-interference effects such as PIR are manifest and moderate efficiency is nevertheless possible.

Although it is relatively easy to surpass the Lambertian limit over a narrow range of frequencies and angles of incidence, it is a challenging task when the entire solar spectrum and a wider angular range are considered. Slanted conical-pore photonic crystals achieve this difficult goal using multiple resonances in the 800–1100 nm wavelength range. These exhibit PIR and vortex-like flow inside the thin-silicon PhC.[33] For 1 μm equivalent bulk-thickness of c–Si, the optimal base-diameter of the slanted cone is 1000 nm and lattice constant of the PhC is 850 nm. This PhC architecture, backed by an Ag back-reflector, yields a MAPD of 35.5 mA/cm^2 over the 300–1100 nm wavelength range, exceeding the Lambertian limit of 32.86 mA/cm^2 for 1 μm-thick c–Si. This study also shows that the response of the slanted conical-pore PhC is extremely robust with respect to the angle of incidence and the

absorption does not exhibit any substantial degradation at least up to an off-normal incidence angle of 50° for all polarizations. This extreme robustness of slanted-cone PhC is due to the PIR modes that exhibit similar robustness for a wide range of angles of incidence.[32] x–y symmetry-breaking slanted conical-pore PhC enables better light-trapping than its vertical counterpart. This was illustrated in Ref. 33 by comparing the performances of the slanted and vertical conical-pore PhCs placed on semi-infinite glass substrates. These ultra-thin silicon structures demonstrate the possibility of solar light-trapping and absorption beyond the Lambertian limit over the entire 300–1100 nm wavelength range. However, they are difficult to fabricate on a large scale and the required pore shapes may give rise to unwanted surface recombination centers of photo-generated charge carriers. Nevertheless, assuming a SRV of 100 cm/s throughout the top Si–SiO$_2$ interfaces and a bottom contact SRV of 10^5 cm/s, a projected efficiency of 17.5% was predicted[42] for a silicon film with only 1 μm equivalent bulk thickness. This efficiency improves to 22.5%[42] if the bottom contact SRV is reduced to 100 cm/s. In these calculations, a detailed treatment of Auger and Shockley–Read–Hall carrier recombination was not undertaken. Instead, it was assumed that the combined effect of these recombination processes simply led to an overall carrier diffusion length of about 10 μm.

Similar considerations apply to other direct bandgap semiconductors such as gallium arsenide. Eyderman and John[88] illustrated absorption of almost 90% of the incident sunlight over the 300–865 nm wavelength range in a slanted-conical pore PhC with 200 nm equivalent bulk-thickness of GaAs. The slanted conical-pores have a base-diameter of 600 nm, pore-depth of 290 nm, and lattice constant of 550 nm. In contrast to silicon, GaAs is a direct bandgap material and susceptible to significant radiative recombination. The photons emitted due to radiative recombination can be reabsorbed by the GaAs cell. This is known as photon-recycling. In the absence of photon-recycling and for 1000 cm/s SRV, the slanted-conical pore GaAs cell yields 28.3% power conversion efficiency with a MAPD of 27.6 mA/cm^2. With complete photon-recycling and the same SRV, the conversion efficiency increases to 29%. Surface passivation for GaAs is more difficult than for silicon, and it may be practically unfeasible to achieve SRV below 1000 cm/s. If the SRV is hypothetically reduced to 10 cm/s, the conversion efficiency of the ultra-thin cell would reach 30.6%. Although slanted-conical pore PhC's exhibit excellent light-trapping capability and beyond-Lambertian limit absorption, fabrication of such structures is difficult and may require advanced nano-imprinting and deposition techniques. Due to the direct bandgap of GaAs, photonic crystal light-trapping serves primarily to reduce the thickness of the cell by about a factor of 10 from the current world-record holding cell from Alta Devices.[7] Efficiencies beyond the current 29.1% would require improvements to state-of-the-art surface passivation.
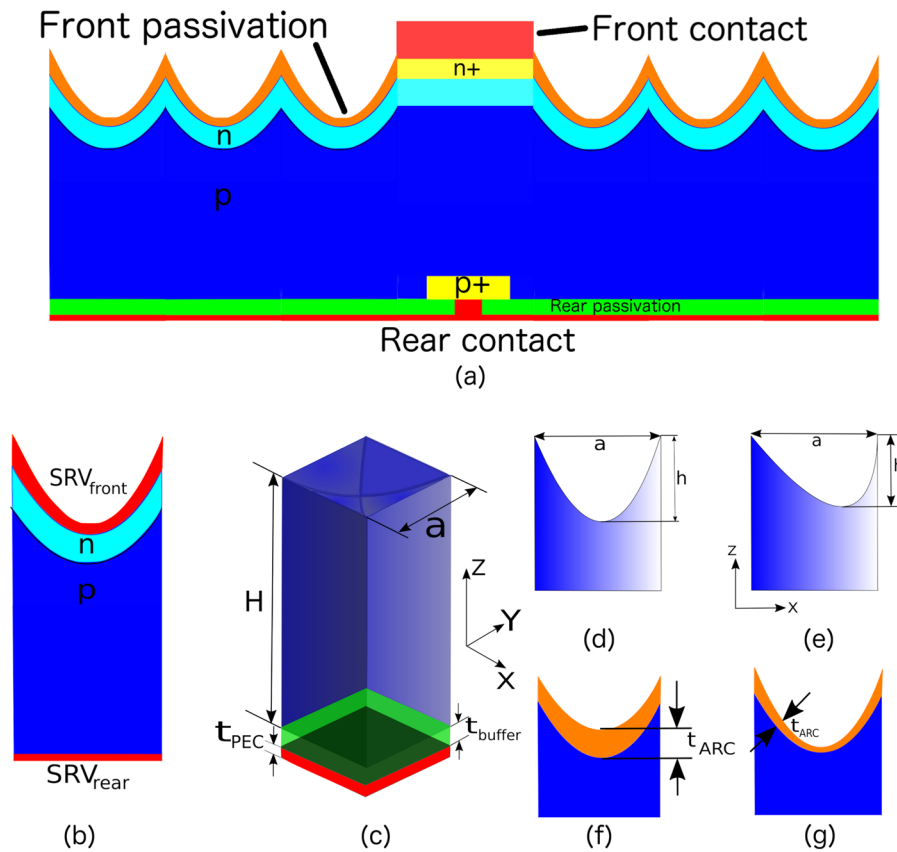

FIG. 2. Architecture of a parabolic-pore PhC solar cell (not to scale): (a) cross-sectional view of the 3D cell and (b) model used for carrier transport calculations. The details of the contact and passivation geometries, effect of passivation, BSF, etc., are subsumed in SRV_{front} and SRV_{rear}. (c) Unit cell of the parabolic-pore PhC used for FDTD computation. The red and green slabs underneath the cell represent the SiO$_2$ buffer layer and the PEC back-reflector, respectively. (d) and (e) show the xz-view of the vertical and slanted parabolic pores, respectively. The yz-view of both architectures are same as (d). A slanted-parabolic-pore PhC that breaks the xy-symmetry enables better light-trapping performance in comparison with the vertical parabolic-pore PhC. (f) and (g) show the non-conformal and conformal ARC layers, respectively. Non-conformal ARC is thicker near the bottom of the pore and results in a better anti-reflection property than the conformal one.

The requirements that thin-film silicon PhCs absorb light beyond the Lambertian limit and at the same time are amenable to existing fabrication techniques lead us to parabolic-pore and inverted micro-pyramid architectures. Using reactive ion etching (RIE), Kuang et al. fabricated 10 μm-thick c–Si parabolic pore PhC with 1200 nm lattice constant and 60 nm anti-reflection coating (ARC) of SiO$_2$.[48] In this PhC architecture, each pore has a depth to lattice constant ratio of 0.65. FDTD computations exhibit excellent agreement with the measured absorption of this PhC and reveal a MAPD of 39.1 mA/cm^2, slightly below the Lambertian limit of 39.65 mA/cm^2 in a 10 μm c–Si slab. High resolution FDTD simulations also reveal a high density of resonances due to PIR in the near-infrared spectrum. This structure combines a graded-index anti-reflection property and strong absorption of sunlight through wave-interference based light-trapping. An experimentally feasible way to enhance the light absorption is by simultaneously optimizing the pore-height (h) and lattice constant (a) of the PhC.[49] This (h/a) ratio is crucial to optimizing light-trapping. For a more graded-index and anti-reflection, a larger (h/a) is desirable. However, deeper pores imply less light-absorbing material. Figure 2(a) shows a schematic of the parabolic-pore PhC based solar cell design proposed in Ref. 49. This passivated emitter rear contact (PERC) cell has a conformal n-type region of width $t_{emitter}$ with a doping density N_d and a p-type base region with a doping density N_a. The combination of the perfect electric conductor (PEC) layer of thickness t_{PEC} = 100 nm and SiO$_2$ buffer layer of thickness t_{buffer} = 75 nm underneath the cell acts as a back-reflector of the cell and improves the optical performance of the cell. If the PEC layer is replaced by a 100 nm thick Ag layer, the same MAPD is obtained, provided the buffer layer exists between the silicon and the Ag layer.[49] This buffer layer also acts as rear passivation to the cell. The bottom contact touches the active silicon region through highly p-doped (p^+) back surface field (BSF) regions. Similarly, the front SiO$_2$ anti-reflection coating (ARC) of thickness t_{ARC} provides front passivation. The front electrodes of the cell, made of either indium tin oxide (ITO) or metal, make contact to c–Si through highly n-doped (n^+) regions, diffused at a regular spacing determined by the emitter-pitch of the cell.

The optimization map of Fig. 3 (assuming t_{buffer} = 75 nm and no ARC), obtained from 3D FDTD computations using the Electromagnetic Template Library (EMTL),[89] shows that the optimum
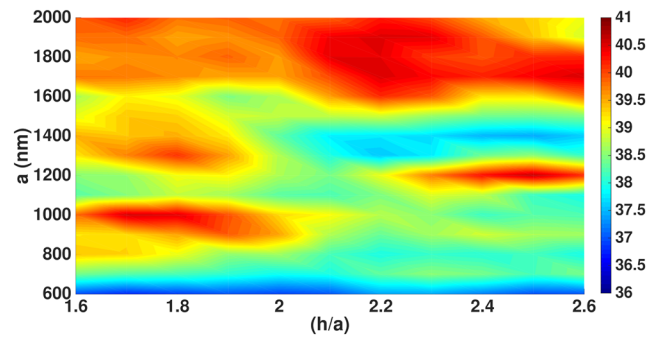

FIG. 3. MAPD optimization in 10 μm-thick vertical parabolic-pore silicon PhC with t_{PEC} = 100 nm, t_{buffer} = 75 nm, and t_{ARC} = 0. An optimum MAPD of 40.57 mA/cm^2 is obtained for a = 1000 nm and (h/a) = 1.8.

design parameters for the 10 μm-thick c–Si parabolic-pore PhC are a = 1000 nm and (h/a) = 1.7. This provides a MAPD of 40.57 mA/cm^2, already more than the Lambertian limit of 39.65 mA/cm^2. With a 50 nm thick non-conformal ARC layer of SiO$_2$, this MAPD improves to 41.09 mA/cm^2. As in the case of conical-pore PhC,[33] a further improvement in the light absorption of the parabolic-pore PhC can be achieved by tilting the pores slightly and breaking the x–y symmetry of the crystal. An optimum tilt angle of θ = 10° enhances the light absorption in the 750–1000 nm wavelength range of the solar spectrum (see Fig. 4) and yields MAPD of 41.72 mA/cm^2.[49] The solid blue circle in Fig. 4 corresponds to the 97.4% absorption peak at λ = 940 nm for the slanted parabolic-pore PhC. In comparison with this, the vertical parabolic-pore PhC absorbs 86.7% light at this wavelength.

The underlying mechanism for the better light-trapping is illustrated through comparison of the in-plane Poynting vector flows of the vertical and tilted pore structures.

Figure 5 depicts energy density distributions and in-plane components of the Poynting vectors along orthogonal slices for y-polarized incident light. The energy densities are normalized by the incident energy density. Figures 5(a) and 5(c) show the Poynting vector flow at λ = 940 nm in the central xz- and yz-planes of the vertical parabolic-pore PhC unit cell. Similarly, Figs. 5(b) and
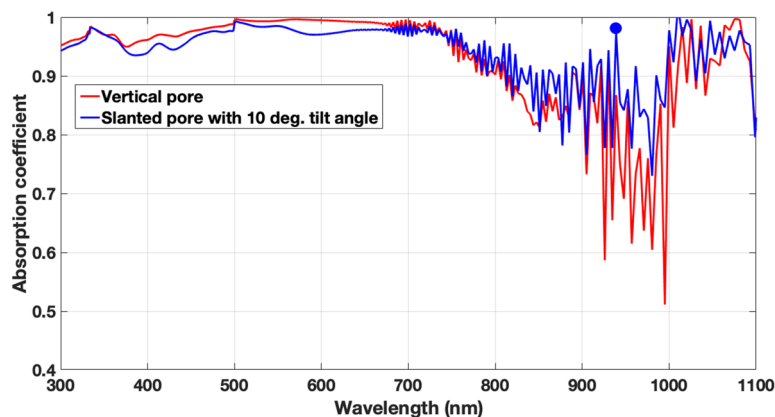

FIG. 4. Comparison of absorption spectra of the vertical and slanted parabolic-pore PhC structures under y-polarized excitation. For both PhCs, t_{buffer} = 75 nm, t_{ARC} = 0, and t_{PEC} = 100 nm. The x–y symmetry-breaking PhC absorbs more light in 750–1000 nm wavelength range.
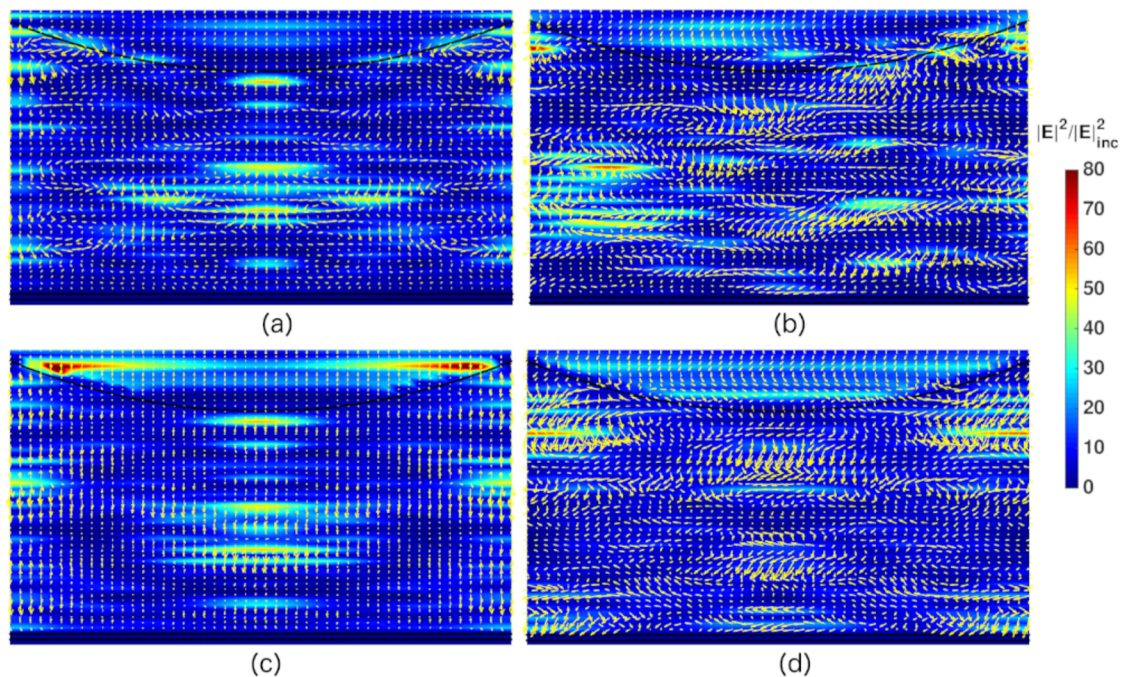
FIG. 5. Plot of energy density and in-plane Poynting vector for vertical and slanted pore PhCs at λ = 940 nm. The incident plane wave is polarized along the y-direction. (a) and (b) correspond to the xz-slice (passing through the center of the unit cell) for vertical and slanted pores, respectively. The Poynting vectors show significant parallel-to-interface power flow and prominent formation of vortices in (b) as compared to (a). (c) and (d) show the central yz-slice for the vertical and slanted pores, respectively. For the vertical pores almost all the power flows from top to bottom. However, (d) shows prominent vortices in the power flow pattern and parallel-to-interface Poynting vectors. Clearly, PIR into slow-light modes is a key mechanism for better light-trapping in the x–y symmetry-broken structure.

5(d) correspond to the Poynting vector flow at the same wavelength in the central xz- and yz-planes of the slanted-pore PhC unit cell. The colormap in these plots corresponds to the intensity enhancement (normalized by incident intensity) in the PhC. A comparison of Figs. 5(a) and 5(b) reveals that the vertical parabolic-pore PhC exhibits fewer intensity hotspots caused by wave-interference and less parallel-to-interface and vortex-like energy flow in comparison with the slanted-pore PhC. This distinction becomes more stark in the yz-plane energy flows, shown in Figs. 5(c) and 5(d). For the x–y symmetric PhC, almost all the incident energy flows along the z-direction. When the x–y symmetry is broken, the Poynting vector exhibits considerable parallel-to-interface energy flow and vortex-like patterns near the intensity hotspots.[49] The resulting long dwell time of photons within the active region facilitates carrier generation even when the intrinsic absorption of silicon is weak. Parallel-to-interface and vortex-like flow of light is the result of multiple coherent scattering and wave-interference. They cannot be captured in a ray-optics approximation. The Lambertian distribution predicts negligible probability for ray propagation nearly parallel to the air-silicon interface. In contrast, an accurate solution of Maxwell's equations shows that parallel-to-interface and vortex-like energy flows are very prominent in well-designed photonic crystals beyond 700 nm wavelength. These and other slow-light modes enable thin-silicon PhC structures to absorb sunlight beyond the Lambertian limit. 1D charge carrier transport calculation reveals that a 10 μm-thick slanted parabolic-pore PhC solar cell is capable

of achieving 28%–29% power conversion efficiency when including absorption only in the 300–1100 nm range.[49] However, this efficiency does not include practical effects such as electronic BGN[50] and phonon-assisted sub-bandgap absorption associated with the Urbach tail.[51–54]

While parabolic-pore structures are amenable to microfabrication, the reactive-ion etching method may cause substantial damage to the silicon crystal structure below the top surface. The resulting electronic defects may lead to considerable non-radiative carrier recombination in the bulk. The slightly overlapping pores in the structure (optimized for light-trapping) lead to intricate teepee-like protrusions that may likewise act as surface recombination centers. Both of these effects, without any further treatment, may lead to short carrier lifetime and reduce the solar cell efficiency. It is, therefore, vital to consider architectures in which both light-trapping and electronic properties can be optimized.

IV. MICRO-PYRAMID PHOTONIC CRYSTAL DESIGN OPTIMIZATION

A more likely candidate for high efficiency silicon solar cells consists of inverted-micropyramid PhCs. These can be fabricated with a high accuracy through masking and wet-etching of c–Si. Due to the anisotropic etching property toward c–Si, KOH readily etches and exposes the (111) and related surfaces of silicon, leading to formation of inverted-pyramids with a side-wall angle of 54.7°, the

angle between (111) and the initial (100) planes of c–Si. A detailed FDTD based light-trapping optimization study[44] of silicon inverted-micropyramid PhCs showed that a 10 μm-thick structure with a lattice constant of 2500 nm and 200 nm SiO$_2$ ARC enables MAPD of 42.5 mA/cm^2, significantly surpassing the Lambertian limit. This architecture differs from the classical inverted-pyramid PERL cells, used to achieve an early world-record efficiency,[2] in two important ways. The first is the choice of the pyramid base length and corresponding pitch of the square lattice array. The second is the thin and flexible nature of the PhC architecture. Unlike the classic PERL cell pyramids with base lengths on the order of 10 μm, the photonic crystal micro-pyramids focus on base lengths and lattice constant in the range of 1–3 μm, much closer to the wavelength of sunlight. This reduction in length scales leads to dramatically different wave-interference based light-trapping effects that are absent in the classic structures that rely on ray-optics based light-trapping. The result is that a 10 μm-thick silicon micro-pyramid PhC can absorb as much light as a 400 μm-thick classic inverted-pyramid PERL cell. This dramatic reduction in thickness, while not sacrificing solar-absorption, has the major consequence that bulk, non-radiative charge carrier recombination (including Auger recombination) is substantially reduced. The inverted micro-pyramid PhC has the advantage over previously discussed PhC architectures in that the exposed (111) face of silicon is amenable to high-quality surface passivation. In other words, the micro-pyramid PhC enables both state-of-the-art electronic quality and beyond-Lambertian light-trapping.

The optical and electronic modeling of inverted micro-pyramid PhCs, made from 3 μm to 20 μm-thick c–Si, has been reconsidered in recent works.[46,47] Two types of inverted micro-pyramid PhC solar cell architectures, PERC (similar to the parabolic-pore PhC solar cell shown in Fig. 2) and interdigitated back-contact (IBC) cells, are shown in Figs. 6(a) and 6(c), respectively. The PERC architecture features 10–20 μm-wide metal contacts at the top of the cell. These metal contacts block a part of the incoming sunlight, leading to "shadowing loss" in the cell. Experimental measurements[90] have shown that a front-contact geometry with 20 μm finger-width and 800 μm finger-spacing leads to ~1% shading loss of the photocurrent in the solar cell. The loss in the conversion efficiency of the cell is roughly the same as this percentage shading loss. Some recent design and experiments of "cloaked contacts" have shown that a major fraction of this loss can be overcome by redirecting the light around the contacts.[91–94] A more reliable way to eliminate the shading loss is to place all the contacts at the rear surface of the cell, leading to the IBC architecture.[95–97] The most recent world-record holding Kaneka cell[6] uses the IBC architecture. In addition to shading-loss, the PERC architecture also suffers from loss in power conversion efficiency due to sheet-resistance. The carriers, entering the emitter region of the cell, must travel a long lateral distance of several hundreds of micrometers between the front electrodes
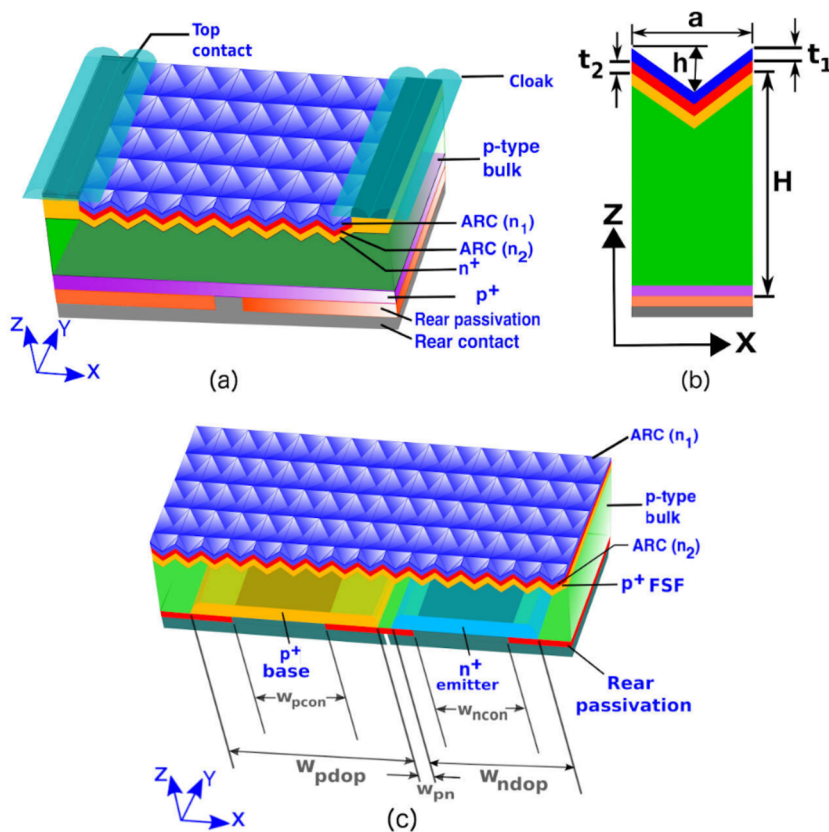

FIG. 6. Geometry of an inverted pyramid PhC solar cell (a) PERC architecture: cloaking of top-contact could be a possible way to reduce shading loss. (b) 2D cross section of a unit cell of the inverted micro-pyramid PhC showing FDTD design parameters. The side-wall angle of the wet-etched pyramid is 54.7° [i.e., $h/(a/2) = \tan 54.7°$]. The thickness of the active layer is H. (c) IBC architecture: the widths of the highly doped p^+ and n^+ regions at the back of the cell are w_{pdop} and w_{ndop}, respectively. The edges of these regions are separated by a distance w_{pn}. The base and emitter contact-widths are w_{pcon} and w_{ncon}, respectively. The front p^+ layer acts as the front surface field.

through the thin emitter-sheet before they can be collected. The corresponding resistance contributes to a loss in the conversion efficiency. While it is tempting to reduce the sheet-resistance by increasing the emitter-thickness, doing so would also cause more Auger recombination of carriers. In order to balance the Auger recombination and sheet-resistance loss, an optimum emitter-design must be chosen for a PERC cell. On the other hand, when the emitter and base contacts are placed alternately in the IBC cells, they do not suffer substantial loss in efficiency due to emitter resistance. Overall, the IBC design provides better solar absorption, eliminates sheet resistance losses, and improves overall charge carrier collection, leading to the highest possible solar cell efficiencies.

Figures 6(a) and 6(c) show the geometries of inverted micro-pyramid PhC thin c–Si solar cells with PERC[46] and IBC architectures,[47] respectively. Both cell architectures follow the same light-trapping optimization procedure. The PhC has a lattice constant a. The side-wall angle (α) of each pyramid is 54.7°, determined by the anisotropic etching of KOH. The height, h, of each pyramid is given by $h = (a/2)\tan\alpha$. The c–Si active layer thickness (H) is considered in the 3–20 μm range. The front surface of the cell is covered with two conformal ARC layers of refractive indices n_i and thicknesses t_i, where $i = 1$ and 2 correspond to the top and bottom layers, respectively. The ARC layers also act as front passivation for the cell. The electrode fingers make contact with the c–Si layer through highly doped regions with donor (n^+) and acceptor (p^+) impurities. The strong electric field between the highly doped, thin n^+ layer and p-type bulk keeps the minority carriers (holes) away from the emitter electrodes and helps in efficient collection of the photo-generated electrons. Similarly, the p^+ layer acts as the BSF region, leading to efficient collection of holes in the base electrodes. The Gaussian doping profiles of the n^+ and p^+ regions are characterized by $N_i = N_{i0}\exp(-z^2/2\sigma_i^2)$, where N_{i0} denotes the peak concentration (in cm^{-3}) of the dopant species, σ_i is the Gaussian widths (in nm), and $i = n$ and p for the n^+ and p^+ regions, respectively. For both cells, the bulk p-region is assumed to have a uniform acceptor doping concentration (N_A) of 5×10^{15} cm^{-3}. The top contacts of the PERC cell are assumed to be cloaked. The IBC cell has a p^+ front surface field (FSF) layer below the front-passivation. The p^+ and n^+ regions of the IBC cell that cover the base and emitter contacts have widths w_{pdop} and w_{ndop}, respectively, and are separated by a distance w_{pn}. Parts of the back-reflectors protrude through the rear passivation into the silicon and form base and emitter contacts. The widths of the base and emitter contacts are denoted by w_{pcon} and w_{ncon}, respectively.

In FDTD calculations, c–Si is modeled according to a modified Lorentz model over the 300–1100 nm wavelength range.[98]

However, external quantum efficiency (EQE) measurements show that c–Si solar cells are capable of collecting carriers generated by light absorption up to 1200 nm.[99–104] This sub-bandgap absorption in c–Si originates from two mechanisms. The first one is carrier concentration dependent BGN in silicon. This is modeled using Schenk's model[50] and allows absorption of sunlight up to 1120 nm.[46] The absorption up to 1200 nm in c–Si, demonstrated by the EQE measurements, originates from the exponentially decaying Urbach optical absorption edge below the continuum band edge.[51,52] Static disorder in non-crystalline solids leads to an exponential band tail of localized states below the electronic band edge. However, in c–Si, a similar tail of phonon assisted optical absorption generates mobile electron–hole pairs.[53,54] The sub-gap absorption is characterized by an exponential, $\alpha(\nu) \sim \exp[\{h\nu - E_G(T)/E_0(T)\}]$, where ν is the frequency of sunlight, $E_G(T)$ is the downshift of the continuum band edge corresponding to BGN, and $E_0(T)$ is the Urbach slope. Cody et al. measured the Urbach slope of c–Si at 300 K as 8.5 ± 1.0 meV. Microscopic modeling of the optical-absorption edge, taking into account the roles of both acoustic and optical phonons, predicts a slope of 8.6 meV.[53,54] In order to accurately model this sub-bandgap absorption, the experimental absorption coefficient from Ref. 105 is fitted with a series of the form $\epsilon(\omega) = \epsilon_\infty + \sum_j \frac{\triangle\epsilon_j \omega_{pj}^2}{(\omega_{pj}^2 - 2i\omega\gamma_j - \omega^2)}$, where each term of the summation represents a Lorentz oscillator. The fitting parameters ϵ_∞, ω_{pj}, $\triangle\epsilon_j$, and γ_j (shown in Table I), used in the FDTD computation, are obtained using a freely available MATLAB program.[106] The experimental data are found to exhibit an Urbach slope of 8.6 meV over the 1160–1190 nm wavelength range.[46]

Figure 7(a) shows the MAPD optimizations over the 300–1100 nm wavelength range for the inverted pyramid PhCs with different c–Si thicknesses. The front surfaces of the PhCs are coated with optimized dual-layer ARC's with $n_1 = 1.4$, $t_1 = 45$ nm, $n_2 = 2.6$, and $t_2 = 100$ nm.[46] We tabulate the details of the optimization results, along with the MAPD gain, due to sub-bandgap absorption in the 1100–1200 nm wavelength range in Table II. We also include the MAPD corresponding to the Lambertian limit for different values of c–Si thickness. This shows that for each cell-thickness over the 3–20 μm range, the MAPD of inverted micro-pyramid PhC surpasses the Lambertian limit by a significant margin. In Figs. 7(b) and 7(c), we compare the Lambertian absorption spectra (plotted in red) with those of the optimized inverted micro-pyramid PhCs (plotted in blue) for $H = 15$ μm and 5 μm.[47] The PhC absorption spectra exhibit significant light absorption through high densities of resonance peaks in the 950–1200 nm wavelength range. Figure 7(d) shows the Poynting vector flow at $\lambda = 1176$ nm along the central

TABLE I. Fitting parameters used to model Si dispersion data of Ref. 105 in the 1000–1200 nm wavelength range.

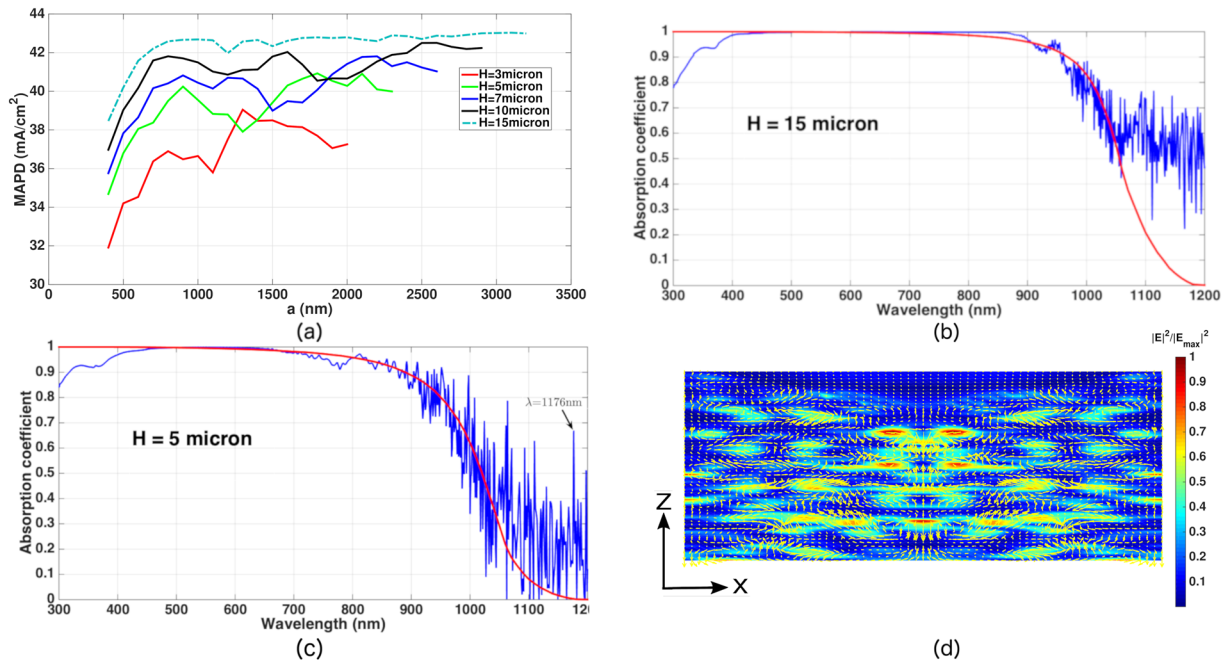| Wavelength range (nm)	ϵ_∞	$\triangle\epsilon_j$	ω_{pj} ($\times 10^3$ μm^{-1})	γ_j ($\times 10^3$ μm^{-1})
		0.971 156	0.001 805	0.000 000
		7.244 785	0.006 785	0.000 001
1000–1200	1.0	0.000 580	0.001 018	0.000 047
		2.519 084	0.002 291	0.000 000
		−0.057 262	0.001 237	0.000 004

FIG. 7. Light-trapping in inverted pyramid c–Si photonic crystal solar cells. (a) MAPD optimization in the 300–1100 nm wavelength range for different cell-thicknesses (H). Each cell has dual-layer ARCs with n_1 = 1.4, t_1 = 45 nm, n_2 = 2.6, and t_2 = 100 nm. Absorption spectra of the optimized inverted pyramid photonic crystals: (b) H = 15 μm and (c) H = 5 μm. (d) In-plane Poynting vector flow at λ = 1176 nm along the central xz-plane of the 5 μm-thick, optimized PhC unit cell. This wavelength corresponds to a resonant peak in the absorption spectrum of the 5 μm-thick photonic crystal.

xz-plane of the 5 μm-thick, optimized PhC unit cell. This wavelength corresponds to a sharp resonance peak in the PhC absorption spectra of Fig. 7(d). The Poynting vector plot reveals parallel-to-interface and vortex-like energy-flow, indicative of wave-interference based light-trapping.

It is worthwhile asking at this point whether all of the absorption predicted in the 1100–1200 nm range is in fact useful to the

purpose of generating photo-current. Absorption that occurs in sub-gap, localized, electronic states (arising from static disorder) may only lead to rapid charge carrier recombination. However, subgap absorption that is assisted by simultaneous phonon absorption can elevate the excited electron into extended photo-current carrying levels. In order to address this issue, we provide in Table III a compilation of partial MAPD's for different choices of absorption

TABLE II. Summary of wave-interference based light-trapping optimization in 3–20 μm-thick inverted pyramid PhC solar cells considered in Refs. 46 and 47. The inverted-pyramid PhC solar cells are assumed to have dual-layer ARCs with n_1 = 1.4, t_1 = 45 nm, n_2 = 2.6, and t_2 = 100 nm. Each of our inverted pyramid photonic crystals, optimized through stable and accurate solutions of Maxwell's equations, has MAPD considerably above the Lambertian limit. [Reproduced with permission from S. Bhattacharya and S. John, Sci. Rep. **9**, 12482 (2019). Copyright 2019 Author(s), licensed under a Creative Commons Attribution 4.0 license.]

H (μm)	a (nm)	MAPD corresponding to the Lambertian limit (mA/cm^2), 300–1200 nm range	MAPD of an inverted pyramid PhC solar cell (mA/cm^2), 300–1100 nm range	MAPD of an inverted pyramid PhC solar cell (mA/cm^2), 1100–1200 nm range	Total MAPD of an inverted pyramid PhC solar cell (mA/cm^2), 300–1200 nm range
3	1300	36.64	39.05	0.31	39.36
5	1800	38.03	40.93	0.63	41.56
7	2100	38.85	41.81	0.98	42.79
10	2500	39.63	42.50	1.09	43.59
12	2700	40.01	42.75	1.24	43.99
15	3100	40.44	43.03	1.36	44.39
18	1900	40.78	43.11	1.34	44.45
20	2900	40.97	43.12	1.39	44.51

TABLE III. Partial MAPDs and projected conversion efficiencies corresponding to different choices of cutoff wavelength for a 15 μm-thick inverted-pyramid PhC solar cell. Consideration of subgap phonon-assisted absorption over the entire 1100–1200 nm range yields an extra MAPD of 1.36 mA/cm^2 and 31.07% conversion efficiency for the 15 μm-thick cell. However, if the subgap absorption is completely neglected, the projected conversion efficiency still surpasses 30%. A detailed description of the electronic properties of the solar cell leading to these projected efficiencies is given in Sec. V.

Cutoff wavelength (nm)	Partial MAPD (mA/cm^2)	Projected efficiency (%)
1100	43.03	30.12
1120	43.16	30.20
1140	43.31	30.32
1160	43.53	30.47
1180	43.96	30.77
1200	44.39	31.07

wavelength cutoff. This is presented for the case of the 15 μm-thick cell for cutoff wavelengths ranging from 1100 to 1200 nm. The conditions leading to the projected power conversion efficiencies are described in the following section.

V. ELECTRONIC PERFORMANCE OF THIN-FILM PHOTONIC CRYSTAL SOLAR CELLS

In this section, we illustrate the electronic performances of various PhC solar cells through numerical solutions of the 1D and 2D Poisson's equation, coupled with semiconductor drift-diffusion equations. The numerical calculations are performed using Sentaurus.[107] We review 1D and 2D transport calculations for the inverted pyramid PhC PERC cell and 2D transport calculations for the IBC cell. These 1D and 2D charge carrier transport calculations have been shown to agree well with more demanding 3D calculations.[46] For 1D transport calculations, MAPDs from 3D FDTD computations are used to obtain an equivalent generation profile according to an algorithm and the efficiency is corrected for sheet resistance losses.[49] For 2D transport calculations, the actual generation profiles obtained from the 3D computations are integrated along one of the lattice directions. The resulting 2D profiles are then repeated over many PhC unit cells to cover the large scale contact geometry used in the Sentaurus computations. The 2D carrier generation profiles for the optimized inverted pyramid PhCs with H = 3 μm, 5 μm, 7 μm, and 10 μm, obtained by integrating the 3D generation profile along the y-direction over a unit cell, are shown in Fig. 8.

The charge carrier transport calculations of thin-silicon PhC solar cells employ various models for bulk and surface recombination.[46,47,49] The bulk-recombination of the carriers takes into account both Auger (implemented using the state-of-the-art Auger model in Ref. 11) and SRH recombination (using a SRH lifetime, τ_{SRH}). Due to significantly reduced bulk recombination enabled by optimized doping of the thin silicon layer, the diffusion length of the charge carriers is much larger than the PhC solar cell thickness. As a result, most of the photo-generated carriers are able to reach the surface of the cells. However, the potential to realize a high-efficiency cell depends on the ability of the cell to collect these carriers before they recombine at the interfaces. Surface passivation is crucial to realize high-efficiency thin-silicon PhC cells. State-of-the-art surface recombination velocities at the oxide-silicon interface typically fall in the range of 1–10 cm/s.[11,108,109] However, the SRV at the metal-silicon contact is much higher. Instead of direct contact to a metal, high efficiency solar cells use
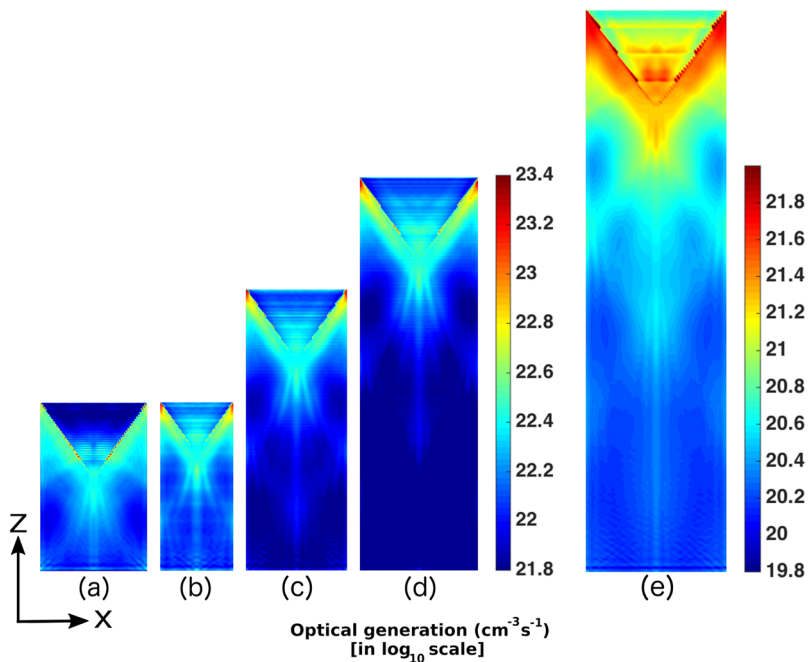

FIG. 8. Carrier generation rate within the unit cell of various inverted pyramid PhC solar cells (integrated along the y-direction):[47] (a) H = 3 μm, a = 1300 nm; (b) H = 5 μm, a = 1800 nm; (c) H = 7 μm, a = 2100 nm; (d) H = 10 μm, a = 2500 nm; and (e) H = 12 μm, a = 2700 nm. The lattice constants correspond to optimized PhCs. In 3D, thin wedges of silicon occur within the triangles, leading to carrier generation throughout the depicted 2D regions.

Optical generation (cm^{-3}s^{-1}) [in log$_{10}$ scale]

carrier-selective heterojunction contacts. These include a stack of intrinsic and p/n-doped hydrogenated amorphous silicon (as employed in the Kaneka cell[6]) or polysilicon on oxide (as employed in the POLO-IBC cell[4]). The SRV at the interface of c–Si and a stack of intrinsic and doped amorphous silicon can be as low as 2–5 cm/s.[110,111] For POLO-IBC cells, the contact SRV ranges between 2 cm/s and 20 cm/s.[5]

In 1D transport calculations, the geometric details of the passivation layers and contacts of the actual 3D cell are subsumed into the equivalent front and rear surface recombination velocities, SRV_{front} and SRV_{rear}.[46,49] These equivalent SRVs appear as boundary conditions in the 1D transport model. For 2D and 3D computations, a more microscopic model is used for the surface recombination at the insulator–Si interface using SRH statistics for the recombination rate,[112]

$$R_{surface}^{SRH} = \frac{\left(n_s p_s - n_i^2\right)}{(n_s+n_i)\big/S_{p0} + (p_s+n_i)\big/S_{n0}}, \quad (5)$$

where $S_{j0} = v_{th,j}\sigma_j D_{interface}$ with $j = n, p$ are microscopic surface recombination velocities ($v_{th,j}$ is the thermal velocity of the electrons/holes, σ_j is the electron/hole capture cross section, and $D_{interface}$ is the interface trap density at the oxide-semiconductor interface), n_s and p_s are the electron and hole concentration at the Si surface, and $n_i = \sqrt{N_e N_h}\exp\left(-E_g(T)\big/2k_B T\right)$. Here, T is the temperature (in K) and $E_g(T)$ denotes the bandgap of Si. N_e and N_h are defined in terms of the electron/hole effective mass m_e^*/m_h^* and Planck's constant h as $N_j = 2\left(\frac{2\pi m_j^* K_B T}{h^2}\right)^{3/2}$ with $j = e$ and h for electrons and holes, respectively. For electrons, $v_{th} = \sqrt{\frac{3KT}{m_e^*}} = 1.12 \times 10^7$ cm/s for $m_e^* = 1.08 m_e$ and $T = 298$ K. The thermal velocity of holes is slightly lower due to higher effective mass ($\sim 1.5 m_e^*$). $D_{interface}$ is set to 3×10^9 cm^{-2} according to the measured value of the near-midgap trap density at the Si-insulator interface in Ref. 113. σ_p is taken to be 6×10^{-17} cm^2 for these traps from the measured data on capture cross sections (Fig. 6 in Ref. 114). This figure also shows that the measured value of σ_n varies over a large range. The choice of $\sigma_n = 6 \times 10^{-16}$ cm^2 results in S_{n0} that closely approximates the effective SRV of state-of-the-art measurements.[11] Accordingly, the choice of $S_{n0} \approx 20.16$ cm/s and $S_{p0} \approx 1.7$ cm/s is made for the 2D transport calculations[46,47] discussed in this review.

TABLE IV. Parameters used in the thickness optimization of the inverted pyramid photonic crystal IBC cell, as described in Fig. 10. The Auger recombination of the carriers is described by the improved Auger model of Ref. 11. The surface recombination at the insulator–Si interface is modeled according to Eq. (5) with $S_{n0} = 20$ cm/s and $S_{p0} = 1.7$ cm/s. [Reproduced with permission from S. Bhattacharya and S. John, Sci. Rep. **9**, 12482 (2019). Copyright 2019 Author(s), licensed under a Creative Commons Attribution 4.0 license.]

Parameters	Description
τ_{SRH}	0.1 ms, 0.5 ms, 1 ms and 10 ms
Contact SRV	10 cm/s
w_{pcon}	140 μm
w_{ncon}	10 μm
w_{pn}	1 μm
w_{pdop}	$1.1 w_{pcon}$
w_{ndop}	$1.1 w_{ncon}$
Bulk acceptor doping	5×10^{15} cm^{-3}
N_{p0}	4×10^{18} cm^{-3}
σ_p	100 nm
N_{n0}	2×10^{18} cm^{-3}
σ_n	220 nm

So far, we have not taken into account carrier-induced bandgap narrowing (BGN) and sub-bandgap absorption in c–Si through the Urbach absorption edge. These effects always exist in a real cell. For conventional solar cells, BGN leads to lowering of the open circuit voltage without any substantial improvement in current. The overall effect is a slight lowering of the cell efficiency. In optimized photonic crystal solar cells, wave-interference based light-trapping provides a more significant increase in photo current that more than offsets the reduction in voltage. The result is a slight increase in efficiency.[46,47] In the 2D transport calculation of Fig. 9, BGN is included using Schenk's model[50] and an accurate description is made of the c–Si optical absorption in the 1100–1200 nm wavelength range (given in Table I). State-of-the-art lifetime measurements[11] show that a good quality c–Si wafer has τ_{SRH} close to 10 ms. Using these parameters, along with an emitter-pitch of 500 μm, a 30.15% conversion efficiency is predicted for the 10 μm-thick, inverted micro-pyramid PhC solar cell with cloaked upper contacts. The corresponding J–V
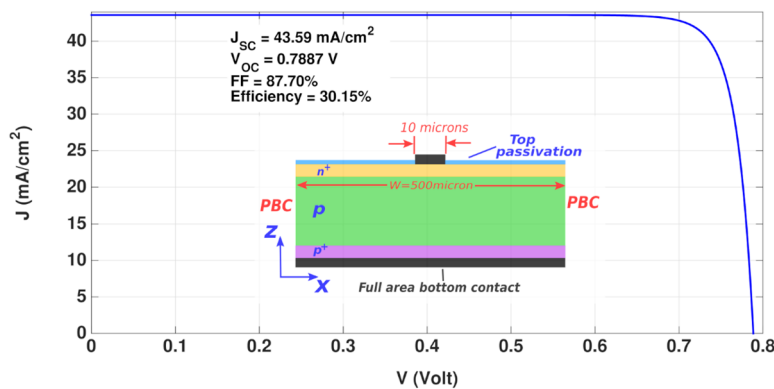

FIG. 9. J–V characteristic for a 10 μm-thick, inverted micropyramid, silicon PhC solar cell, calculated by the 2D transport model.[46] This cell has a full-area bottom contact and 500 μm emitter-pitch. Here, BGN is included and τ_{SRH} = 10 ms. The emitter of the cell has a Gaussian doping profile with a Gaussian width of 205 nm and a peak value of 3×10^{18} cm^{-3}. The p^+ BSF has a Gaussian width of 50 nm and a peak doping of 2×10^{19} cm^{-3}. The top contact is 10 μm wide. The contact SRVs of top and bottom contacts are 10 cm/s. The SRV of the insulator–Si interface is determined according to Eq. (5) with S_{n0} = 20 cm/s and S_{p0} = 1.7 cm/s.
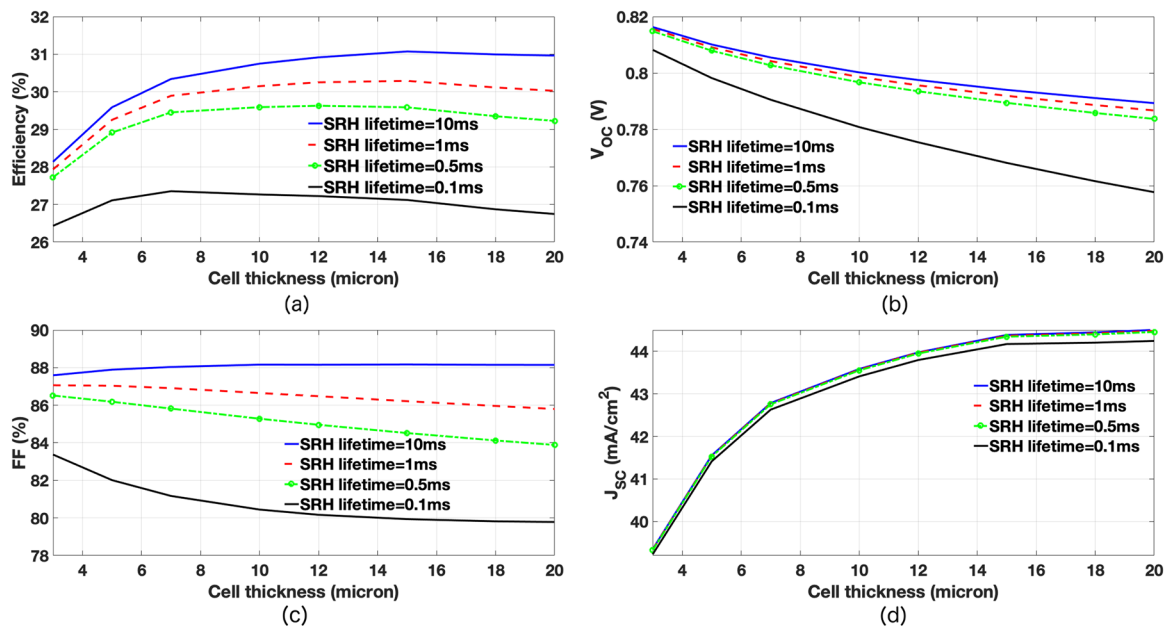
FIG. 10. Thickness optimization of thin-silicon inverted pyramid PhC IBC solar cells with optimum lattice constants and dual-layer ARCs, given by Table II. The cell design parameters for transport computations are given in Table IV. For τ_{SRH} = 0.1 ms and 0.5 ms, the optimum IBC cells are 7 μm and 12 μm thick, respectively. For both τ_{SRH} = 1 ms and 10 ms, the optimum cell-thickness becomes 15 μm.[47]
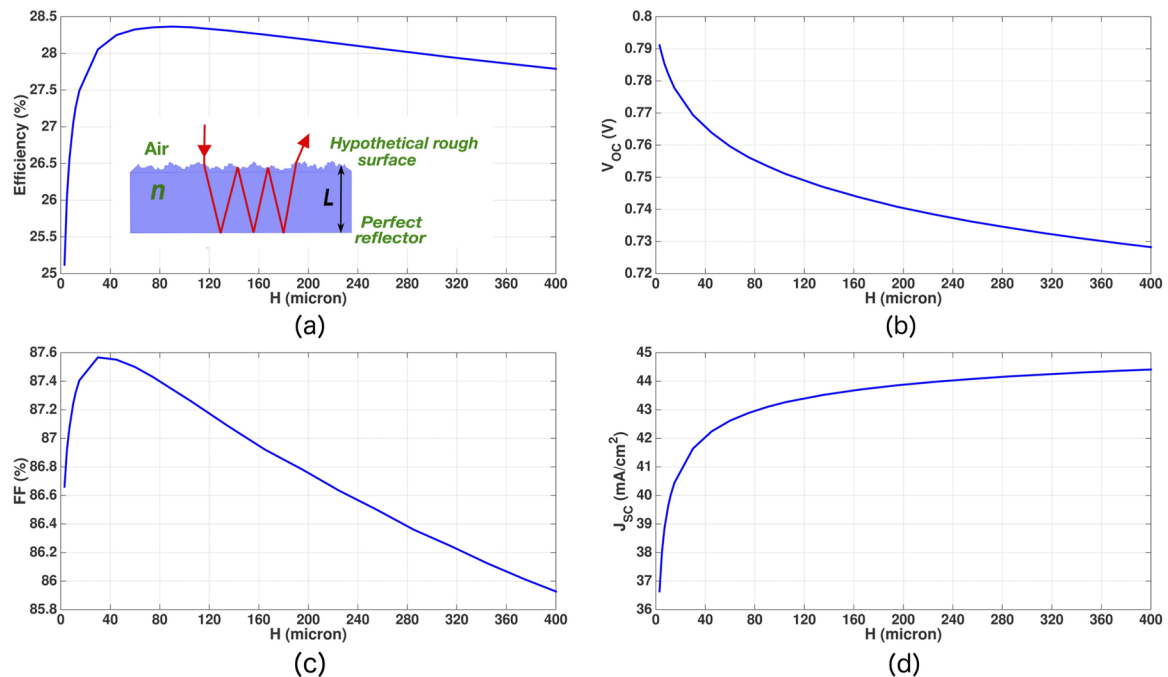

FIG. 11. Thickness optimization of solar cells with Lambertian light-trapping, realistic contact geometry, doping profiles, and recombination parameters. The doping profiles and the contact geometry of the Lambertian IBC cell are the same as the inverted pyramid PhC IBC cell (given by Table IV). The Lambertian cells are assumed to have contact SRV = 10 cm/s, τ_{SRH} = 10 ms, and Auger recombination parameters according to Ref. 11. BGN is modeled according to Ref. 47. In comparison with a lossless, undoped Lambertian cell with a maximum theoretical efficiency of 29.43% and optimum thickness of 110 μm,[9] inclusion of practical doping profiles, bulk recombination, and surface recombination reduces the maximum theoretical efficiency of the Lambertian cell to 28.37% with an optimum thickness of 90 μm. [Reproduced with permission from S. Bhattacharya and S. John, Sci. Rep. **9**, 12482 (2019). Copyright 2019 Author(s), licensed under a Creative Commons Attribution 4.0 license.]

characteristic of the cell is shown in Fig. 9. The inset of the figure shows the 2D transport model of the cell. The cell is assumed to have a full-area bottom contact and 10 μm-wide top contact, both with SRV of 10 cm/s. The emitter has $N_{n0} = 3 \times 10^{18}$ cm^{-3} and a Gaussian width of 205 nm. The p^+ BSF has $N_{p0} = 2 \times 10^{19}$ and a Gaussian width of 50 nm. The surface recombination at the insulator–silicon interface is modeled according to Eq. (5) with S_{n0} = 20 cm/s and S_{p0} = 1.7 cm/s. This realistic cell design shows that the 10 μm-thick, flexible, inverted micro-pyramid PhC cell achieves ~30% efficiency,[46] surpassing the Lambertian efficiency limit of 29.43% (in the presence of BGN)[9] and current world-record efficiency of 26.7% (obtained using an ~16 times thicker cell)[6] by a significant margin.

We now describe the electronic performance of the inverted micro-pyramid PhC cell with an IBC architecture. This architecture is preferred over the PERC architecture due to the absence of shading-loss and sheet-resistance loss. The details of the design parameters of an PhC IBC cell, with a uniform bulk acceptor doping of 5×10^{15} and 1 μm separation between n^+ and p^+ regions at the back of the cell, are shown in Table IV. The parameters such as w_{pcon}, w_{ncon}, N_{p0}, σ_p, N_{n0}, and σ_n are optimized to yield maximum conversion efficiency.[47] The same modeling parameters are used for BGN, sub-bandgap absorption, and surface recombination at the insulator–silicon interface as in the case of the PERC cell.

Unlike the PhC PERC cells, the thickness optimization of the PhC IBC cell is presented for a range of values of τ_{SRH}.[47] The reason for this is that τ_{SRH} is determined by the bulk defects in the c–Si wafer and can vary widely depending upon the quality of the fabrication process. A higher SRH lifetime or lower bulk recombination allows larger solar absorption by using a thicker c–Si layer without losing much photo-current in the recombination process. It follows that for a higher SRH lifetime, the optimum cell-thickness is slightly larger. In Fig. 10, we use τ_{SRH} = 0.1 ms, 0.5 ms, 1 ms, and 10 ms and show the optimum cell-thickness for each case (other simulation parameters appear in Table IV). Figures 10(b)–10(d) show the variation of V_{OC}, J_{SC}, and FF as a function of the cell-thickness. As the cell-thickness is increased from 3 μm to 20 μm, the FF of the IBC cell drops by 4% (additive) for τ_{SRH} = 0.1 ms. As τ_{SRH} increases, the drop in the FF becomes smaller for the same range of cell-thickness variation. For τ_{SRH} = 10 ms, the FF becomes almost independent of cell-thickness. Figure 10(a) shows the variation of the power conversion efficiency of our IBC cell with cell-thickness for different values of τ_{SRH}. For τ_{SRH} = 0.1 ms and 0.5 ms, the optimum IBC cells are 7 μm and 12 μm thick with conversion efficiencies of 27.35% and 29.63%, respectively.[47] For both τ_{SRH} = 1 ms and 10 ms, the optimum cell-thickness becomes 15 μm with power conversion efficiencies of 30.29% and 31.07%, respectively.[47] The better carrier collection capability of the PhC IBC cell boosts the conversion efficiency by
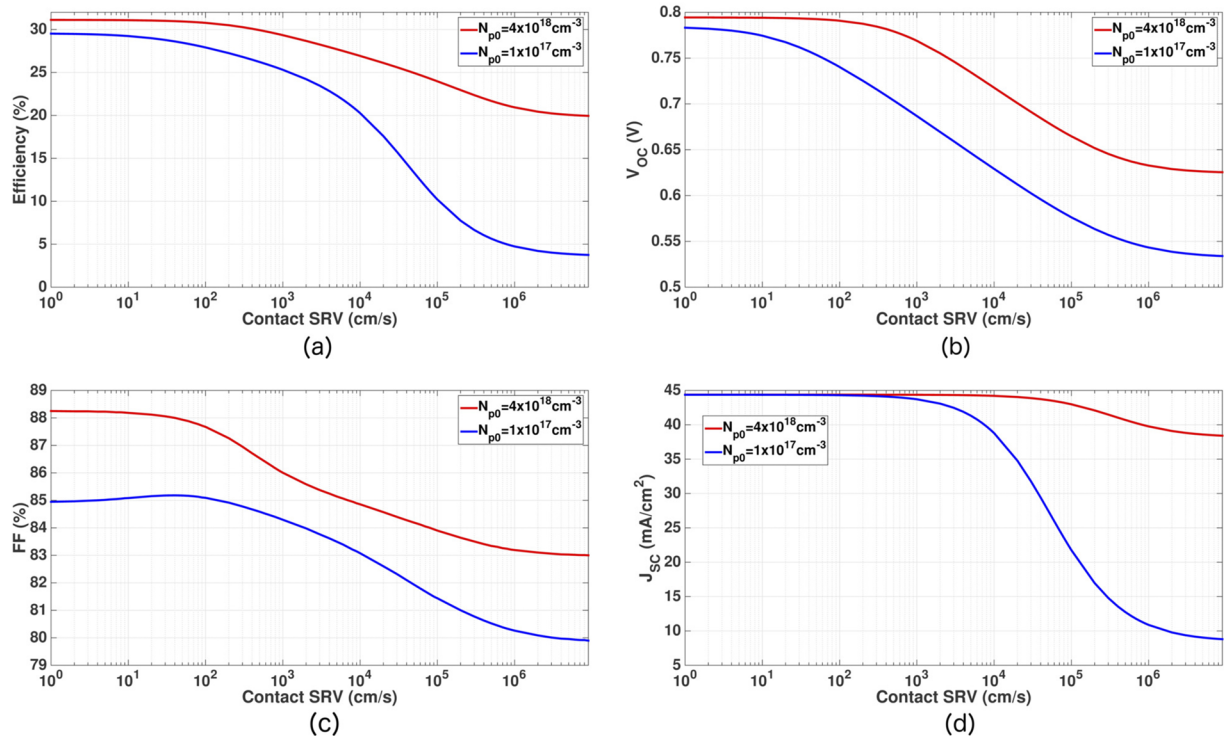

FIG. 12. Effect of contact SRV on the performance parameters of the proposed inverted pyramid PhC IBC cell with H = 15 μm and τ_{SRH} = 10 ms (other design parameters are specified in Table IV). The red curve corresponds to optimum FSF and BSF doping, showing a more gradual drop in the cell efficiency as contact SRV increases. In contrast, a rapid degradation in cell efficiency (blue curve) when FSF/BSF dopings are improperly chosen. [Reproduced with permission from S. Bhattacharya and S. John, Sci. Rep. **9**, 12482 (2019). Copyright 2019 Author(s), licensed under a Creative Commons Attribution 4.0 license.]

1% (additive) in comparison with the PhC PERC cell and leads to a conversion efficiency more than the world-record efficiency of any single-material cell. This also suggests the possibility of a poly-silicon solar cell of 7 μm thickness and $\tau_{SRH} \sim 0.1$ ms, achieving a record efficiency of 27%. Such a cell may be amenable to large-scale, low-cost fabrication through deposition methods.

The 29.43% Lambertian efficiency limit of a silicon solar cell is calculated assuming hypothetical material properties such as no SRH and surface recombination and undoped bulk silicon.[9] To compare the performance of the PhC IBC cell to that of a realistic cell with Lambertian light-trapping, it is necessary to include the same doping profiles, surface recombination, SRH lifetime, and IBC contact geometry as used in the PhC IBC cell. Figure 11 shows the performance parameters of more realistic Lambertian IBC cells of varying thickness, designed according to the parameters of Table IV

and τ_{SRH} = 10 ms. The optimum thickness of the Lambertian cell (with realistic material parameters) is found to be 90 μm with a maximum conversion efficiency of 28.37% in comparison with the optimum 110 μm-thick hypothetical Lambertian cell with 29.43% conversion efficiency. In practice, the light-trapping in the conventional cells falls below the Lambertian limit. This results in an increased optimum thickness of the conventional cells with practical ray-trapping.

In thin-silicon PhC cells with optimized doping configurations, the photo-generated charge carriers travel a small distance in comparison with their diffusion lengths before they are collected at the electrodes. Such cells benefit from low bulk-recombination loss. However, surface recombination remains a very important factor. In Fig. 12, it is shown that the optimization of the FSF and BSF regions plays a paramount role in keeping the minority carriers away

TABLE V. Comparison of the inverted pyramid PhC IBC solar cells with conventional cells at 25 °C. The inverted pyramid PhC cells employ wave-interference based light trapping. The design parameters of the PhC IBC solar cells are given in Table IV. All cells include bandgap narrowing and optical absorption throughout the 300–1200 nm wavelength range.

Cell type/light trapping and transport model	Cell-thickness (μm)	Bulk recombination model	Surface recombination	V_{OC} (V)	J_{SC} (mA/cm^2)	FF (%)	η (%)
Hypothetical Lambertian, undoped[9]	110	Improved Auger,[11] $\tau_{SRH} = \infty$	SRV = 0	0.7613	43.31	89.26	29.43
Hypothetical Lambertian,[47] doping profiles in Table IV	90	Improved Auger,[11] $\tau_{SRH} = 10$ ms	Contact SRVs 10 cm/s	0.7535	43.10	87.34	28.37
Inverted pyramid PhC IBC, 2D transport[47] (design parameters in Table IV)	15	Improved Auger,[11] $\tau_{SRH} = 10$ ms	Contact SRVs 10 cm/s	0.7940	44.39	88.17	31.07
Inverted pyramid PhC IBC, 2D transport[47] (design parameters in Table IV)	15	Improved Auger,[11] $\tau_{SRH} = 10$ ms	Contact SRVs 100 cm/s	0.7908	44.39	87.67	30.77
Inverted pyramid PhC PERC, 2D transport[46] (design parameters of Fig. 9)	10	Improved Auger,[11] $\tau_{SRH} = 10$ ms	Contact SRVs 10 cm/s	0.7887	43.59	87.70	30.15
Kaneka Corporation[6]	165	$\tau = 11.2$ ms $\frac{1}{\tau} = \left(1/\tau_{SRH} + 1/\tau_{surf}\right)$	Included in τ	0.738	42.65	84.90	26.70
POLO (polysilicon on oxide) IBC[4,5]	300	Improved Auger,[11] $\tau_{SRH} = 100$ ms	SRV at front passivation-Si interface = 10 cm/s contact SRV ~ 2–20 cm/s	0.727	42.62	84.28	26.10

from the surface. When this is done correctly, the cell performance is much less sensitive to the SRV. This is illustrated by considering the effect of increased contact SRV on two 15 μm-thick PhC IBC cells: one with optimized and another with non-optimized FSF/BSF. Apart from τ_{SRH} = 10 ms and a variable contact SRV, all other simulation parameters are given by Table IV. Figure 12(a) shows that the power conversion efficiency of the IBC cell with optimized FSF and BSF (i.e., $N_{p0} = 4 \times 10^{18}$ cm^{-3} and σ_p = 100 nm) undergoes only 0.3% (additive) drop, leading to 30.77% efficiency when the contact SRV is increased from 10 cm/s to 100 cm/s (red curves in Fig. 12).[47] In contrast, the blue curve in Fig. 12(a) shows a 5% (additive) drop in the conversion efficiency for the same change in contact SRV, in a cell with inadequate FSF and BSF ($N_{p0} = 1 \times 10^{17}$ cm^{-3} and σ_p = 100 nm in this particular example). When the contact SRVs are extremely high (~10^6 cm/s), the IBC cell with optimum FSF/BSF doping retains ~20% power conversion efficiency. This is in sharp contrast to the cell with inadequate FSF/BSF where the conversion efficiency drops to ~5%. A similar role of BSF is apparent[46] in the case of inverted micro-pyramid PhC PERC cells.

We compare the performance parameters of the thin-silicon inverted micro-pyramid PhC cell with those of the much thicker hypothetical Lambertian cell and the current world-record holding Kaneka cell. The efficiency limit analysis of the hypothetical Lambertian cell assumes no bulk SRH and surface recombination. In addition, the quoted 29.43% efficiency limit corresponds to an undoped bulk silicon.[9] As discussed earlier, a more realistic cell with perfect Lambertian light-trapping would have a lower efficiency. The optimum thickness of a Lambertian cell with a similar doping, SRH recombination, and SRV as the PhC cells described in this article is slightly reduced to 90 μm and has 28.37% power-conversion efficiency. Table V shows that the 15 μm-thick IBC cell, with experimentally attainable design parameters, surpasses the efficiency of a Lambertian cell with a practical carrier transport model by 2.7% (additive). Both inverted micro-pyramid PERC and IBC cells exceed the conversion efficiency of the world-record holding Kaneka cell by ~3.4% (additive) and 4.37% (additive), respectively. In contrast to the Kaneka cell that uses n-type bulk, the recently developed 300 μm-thick POLO-IBC cell[4,5] and the PhC cells reviewed in this article use p-type bulk.

We note finally the consequences of light absorption in the solar cell that might not contribute to photo-current at all. In the optimized 15 μm-thick, inverted micropyramid cell, wave-interference-based light-trapping, in the 1100–1200 nm wavelength range, is predicted to contribute 1.36 mA/cm^2 toward the overall MAPD. Table III summarizes the consequence of removing some or all of this absorption from the carrier generation rate. For all choices of the absorption cutoff wavelength, from 1100 to 1200 nm, the resulting power conversion efficiency remains above 30%.

VI. CONCLUSION

Over the past three decades, light-trapping designs of solar cells have been dominated by ray-optics concepts. Significant progress has been made toward improving wafer quality and contact architectures and reducing surface recombination. However, the light-trapping mechanisms for high-efficiency silicon solar cells have largely ignored the wave nature of light. Despite the progress in electronic properties, the power conversion efficiency has almost

reached a saturation level as evidenced by the 1.7% (additive) efficiency increase in the single-junction silicon solar cells over the past two decades. This review highlights the importance of wave-interference based light-trapping to overcome previously reported barriers to solar absorption and cell efficiency. This wave-interference-based solar absorption is optimized in certain photonic crystal architectures with features on the scale of near-infrared light. In particular, using 10–15 μm-thick inverted micropyramid photonic crystals, it is possible to substantially surpass the Lambertian limit for solar absorption over the 300–1200 nm wavelength range. This opens an unexplored avenue for the realization of single-junction silicon solar cells with a new limiting efficiency of 31%, which is much higher than previous estimates. Remarkably, such high-efficiency silicon solar cells may also be thin and flexible, making them suitable for integration into buildings and other power-consuming devices. Silicon, despite being an indirect bandgap material, is projected to surpass the efficiencies of other direct bandgap materials. The numerically demonstrated power conversion efficiency in the 15 μm-thick PhC-IBC cell is significantly higher than the best thick-silicon cells, such as the 26.7% Kaneka cell and 26.1% POLO-IBC cell, and even higher than the best direct bandgap GaAs cell with 29.1% efficiency.

The efficiency estimate of 31% for the 15 μm-thick silicon PhC solar cell relies on a combination of different factors. These include (i) slightly over 1 mA/cm^2 of useful photocurrent harvested from 1100 to 1200 nm wavelength band, (ii) a carrier lifetime of 10 ms, and (iii) surface recombination velocities on the order of 10 cm/s. However, there is considerable robustness to the prediction of beyond 30% power conversion efficiency. Even if part or all of the sunlight from the 1100–1200 nm band is removed, the projected efficiency remains in the 30%–31% range (see Table III). The same holds true if the carrier lifetime drops to 1 ms [see Fig. 10(a)]. However, as the carrier lifetime is reduced, the optimum thickness of the solar cell is correspondingly reduced. For a more dramatic drop in carrier lifetime to 0.1 ms, the optimum cell-thickness drops to 7 μm and the resulting structure is projected to yield a power conversion efficiency of 27%. Finally, an increase in surface recombination velocity to 100 cm/s still yields above 30% efficiency [see Fig. 12(a)], provided that the silicon doping profiles are chosen appropriately.

Remarkably, the potential efficiency of thin-film silicon PhC solar cells is greater than the numerically predicted[115] efficiency of perovskite–silicon tandem cells and well above the current world-record-holding 28.1% tandem cell demonstrated by Oxford PV.[18] These considerations suggest that single-junction thin-film silicon, aided by wave-interference-based light-trapping, may prove to be among the most fruitful avenues for further research and development in next-generation solar cell technology.

REFERENCES

[1]J. Zhao, A. Wang, and M. A. Green, "24.5% efficiency silicon PERT cells on MCZ substrates and 24.7% efficiency PERL cells on FZ substrates," Prog. Photovoltaics: Res. Appl. 7, 471 (1999).

[2]M. A. Green, "The path to 25% silicon solar cell efficiency: History of silicon cell evolution," Prog. Photovoltaics: Res. Appl. **17**, 183–189 (2009).

[3]M. Taguchi, A. Yano, S. Tohoda, K. Matsuyama, Y. Nakamura, T. Nishiwaki, K. Fujita, and E. Maruyama, "24.7% record efficiency HIT solar cell on thin silicon wafer," IEEE J. Photovoltaics **4**, 96–99 (2014).

[4]F. Haase, C. Hollemann, S. Schäfer, A. Merkle, M. Rienäcker, J. Krügener, R. Brendel, and R. Peibst, "Laser contact openings for local poly-Si-metal contacts enabling 26.1%-efficient POLO-IBC solar cells," Sol. Energy Mater. Sol. Cells **186**, 184–193 (2018).

[5]C. Hollemann, F. Haase, S. Schäfer, J. Krügener, R. Brendel, and R. Peibst, "26.1%-efficient POLO-IBC cells: Quantification of electrical and optical loss mechanisms," Prog. Photovoltaics: Res. Appl. **27**, 950–958 (2019).

[6]K. Yoshikawa, H. Kawasaki, W. Yoshida, T. Irie, K. Konishi, K. Nakano, T. Uto, D. Adachi, M. Kanematsu, H. Uzu, and K. Yamamoto, "Silicon heterojunction solar cell with interdigitated back contacts for a photoconversion efficiency over 26%," Nat. Energy **2**, 17032 (2017).

[7]M. A. Green, Y. Hishikawa, E. D. Dunlop, D. H. Levi, J. Hohl-Ebinger, M. Yoshita, and A. W. Y. Ho-Baillie, "Solar cell efficiency tables (version 53)," Prog. Photovoltaics: Res. Appl. **27**, 3–12 (2019).

[8]W. Shockley and H. J. Queisser, "Detailed balance limit of efficiency of p-n junction solar cells," J. Appl. Phys. **32**, 510 (1961).

[9]A. Richter, M. Hermle, and S. W. Glunz, "Reassessment of the limiting efficiency for crystalline silicon solar cells," IEEE J. Photovoltaics **3**, 1184 (2013).

[10]T. Tiedje, E. Yablonovitch, G. Cody, and B. Brooks, "Limiting efficiency of silicon solar cells," IEEE Trans. Electron Devices **31**, 711 (1984).

[11]A. Richter, S. W. Glunz, F. Werner, J. Schmidt, and A. Cuevas, "Improved quantitative description of Auger recombination in crystalline silicon," Phys. Rev. B **86**, 165202 (2012).

[12]T. Kato, J. Yu, Y. Hirai, H. Sugimoto, and V. Bermudez, "Record efficiency for thin-film polycrystalline solar cells up to 22.9% achieved by Cs-treated C(In,Ga)(Se,S)$_2$," IEEE J. Photovoltaics **9**, 325–330 (2019).

[13]M. Powalla, S. Paetel, E. Ahlswede, R. Wuerz, C. D. Wessendorf, and T. M. Friedlmeier, "Thin-film solar cells exceeding 22% solar cell efficiency: An overview on CdTe-, Cu(In,Ga)Se$_2$-, and perovskite-based materials," Appl. Phys. Rev. **5**, 041602 (2018).

[14]P. Sinha and A. Wade, "Addressing hotspots in the product environmental footprint of CdTe photovoltaics," IEEE J. Photovoltaics **8**, 793 (2018).

[15]J. Ramanujam and U. P. Singh, "Copper indium gallium selenide based solar cells – a review," Energy Environ. Sci. **10**, 1306–1319 (2017).

[16]M. Sessolo and H. J. Bolink, "Perovskite solar cells join the major league," Science **350**, 917 (2015).

[17]W. S. Yang, J. H. Noh, N. J. Jeon, Y. C. Kim, S. Ryu, J. Seo, and S. Seok, "High-performance photovoltaic perovskite layers fabricated through intramolecular exchange," Science **348**, 1234 (2015).

[18]See https://www.nrel.gov/pv/cell-efficiency.html for Best Research-Cell Efficiency Chart, NREL.

[19]S. John, "Strong localization of photons in certain disordered dielectric superlattices," Phys. Rev. Lett. **58**, 2486 (1987).

[20]E. Yablonovitch, "Inhibited spontaneous emission in solid-state physics and electronics," Phys. Rev. Lett. **58**, 2059 (1987).

[21]I. Celanovic, F. O'Sullivan, N. Jovanovic, M. Qi, and J. G. Kassakian, "1D and 2D photonic crystals for thermophotovoltaic applications," Proc. SPIE **5450**, 416 (2004).

[22]W. R. Chan, P. Bermel, R. C. N. Pilawa-Podgurski, C. H. Marton, K. F. Jensen, J. J. Senkevich, J. D. Joannopoulos, M. Soljacic, and I. Celanovic, "Toward high-energy-density, high-efficiency, and moderate-temperature chip-scale thermophotovoltaics," Proc. Natl. Acad. Sci. U. S. A. **110**, 5309–5314 (2013).

[23]Z. Zhou, O. Yehia, and P. Bermel, "Integrated photonic crystal selective emitter for thermophotovoltaics," J. Nanophotonics **10**, 016014 (2016).

[24]Y. Nam, Y. X. Yeng, A. Lenert, P. Bermel, I. Celanovic, M. Soljacic, and E. N. Wang, "Solar thermophotovoltaic energy conversion systems with two-dimensional tantalum photonic crystal absorbers and emitters," Sol. Energy Mater. Sol. Cells **122**, 287–296 (2014).

[25]W. Gu, G. Tang, and W. Tao, "High efficiency thermophotovoltaic emitter by metamaterial-based nano-pyramid array," Opt. Express **23**, 30681 (2015).

[26]M. Suemitsu, T. Asano, T. Inoue, and S. Noda, "High-efficiency thermophotovoltaic system that employs an emitter based on a silicon rod-type photonic crystal," ACS Photonics (2019).

[27]Y. Wang, H. Liu, and J. Zhu, "Solar thermophotovoltaics: Progress, challenges, and opportunities," APL Mater. **7**, 080906 (2019).

[28]L. Ottaviano, E. Semenova, M. Schubert, K. Yvind, A. Armaroli, G. Bellanca, S. Trillo, T. N. Nguyen, M. Gay, L. Bramerie, and J. Simon, "High-speed photodetectors in a photonic crystal platform," in CLEO, San Jose, USA (OSA, 2012), p. CM1A.2.

[29]K. Nozaki, S. Matsuo, T. Fujii, K. Takeda, M. Ono, A. Shakoor, E. Kuramochi, and M. Notomi, "Photonic-crystal nano-photodetector with ultrasmall capacitance for on-chip light-to-voltage conversion without an amplifier," Optica **3**, 483 (2016).

[30]D. H. Choi, S. K. Nam, K. Jung, and J. H. Moon, "2D photonic crystal nanodisk array as electron transport layer for highly efficient perovskite solar cells," Nano Energy **56**, 365–372 (2019).

[31]Q. G. Du, G. Shen, and S. John, "Light-trapping in perovskite solar cells," AIP Adv. **6**, 065002 (2016).

[32]A. Chutinan and S. John, "Light trapping and absorption optimization in certain thin-film photonic crystal architectures," Phys. Rev. A **78**, 023825 (2008).

[33]S. Eyderman, S. John, and A. Deinega, "Solar light trapping in slanted conical-pore photonic crystals: Beyond statistical ray trapping," J. Appl. Phys. **113**, 154315 (2013).

[34]B. Tian, X. Zheng, T. J. Kempa, Y. Fang, N. Yu, G. Yu, J. Huang, and C. M. Lieber, "Coaxial silicon nanowires as solar cells and nanoelectronic power sources," Nat. Lett. **449**, 885–890 (2007).

[35]L. Tsakalakos, J. Balch, J. Fronheiser, B. A. Korevaar, O. Sulima, and J. Rand, "Silicon nanowire solar cells," Appl. Phys. Lett. **91**, 233117 (2007).

[36]T. Stelzner, M. Pietsch, G. Andrea, F. Falk, E. Ose, and S. Christiansen, "Silicon nanowire-based solar cells," Nanotechnology **19**, 295203 (2008).

[37]J. Li, H. Yu, S. M. Wong, G. Zhang, X. Sun, P. G. Lo, and D. Kwong, "Si nanopillar array optimization on Si thin films for solar energy harvesting," Appl. Phys. Lett. **95**, 033102 (2009).

[38]A. Kandala, T. Betti, and A. Fontcuberta, "General theoretical considerations on nanowire solar cell designs," Phys. Status Solidi A **206**, 173–178 (2009).

[39]E. Garnett and P. Yang, "Light trapping in silicon nanowire solar cells," Nano Lett. **10**, 1082–1087 (2010).

[40]G. Demsey and S. John, "Solar energy trapping with modulated silicon nanowire photonic crystals," J. Appl. Phys. **112**, 074326 (2012).

[41]A. Deinega and S. John, "Solar power conversion efficiency in modulated silicon nanowire photonic crystals," J. Appl. Phys. **112**, 074327 (2012).

[42]A. Deinega, S. Eyderman, and S. John, "Coupled optical and electrical modeling of solar cell based on conical pore silicon photonic crystals," J. Appl. Phys. **113**, 224501 (2013).

[43]A. Mavrokefalos, S. E. Han, S. Yerci, M. S. Branham, and G. Chen, "Efficient light trapping in inverted nanopyramid thin crystalline silicon membranes for solar cell applications," Nano Lett. **12**, 2792 (2012).

[44]S. Eyderman, S. John, M. Hafez, S. S. Al-Ameer, T. S. Al-Harby, Y. Al-Hadeethi, and D. M. Bouwes, "Light-trapping optimization in wet-etched silicon photonic crystal solar cells," J. Appl. Phys. **118**, 023103 (2015).

[45]M. S. Branham, W. Hsu, S. Yerci, J. Loomis, S. V. Boriskina, B. R. Hoard, S. E. Han, and G. Chen, "15.7% efficient 10-μm-thick crystalline silicon solar cells using periodic nanostructures," Adv. Mater. **27**, 2182–2188 (2015).

[46]S. Bhattacharya, I. Baydoun, M. Lin, and S. John, "Towards 30% power conversion efficiency in thin-silicon photonic crystal solar cells," Phys. Rev. Appl. **11**, 014005 (2019).

[47]S. Bhattacharya and S. John, "Beyond 30% conversion efficiency in silicon solar cells: A numerical demonstration," Sci. Rep. **9**, 12482 (2019).

[48]P. Kuang, S. Eyderman, M. L. Hsieh, A. Post, S. John, and S. Y. Lin, "Achieving an accurate surface profile of a photonic crystal for near-unity solar absorption in a super thin-film architecture," ACS Nano **10**, 6116–6124 (2016).

[49]S. Bhattacharya and S. John, "Designing high-efficiency thin silicon solar cells using parabolic-pore photonic crystals," Phys. Rev. Appl. **9**, 044009 (2018).

[50]A. Schenk, "Finite-temperature full random-phase approximation model of band gap narrowing for silicon device simulation," J. Appl. Phys. **84**, 3684 (1998).

[51]F. Urbach, "The long-wavelength edge of photographic sensitivity and of the electronic absorption of solids," Phys. Rev. **92**, 1324 (1953).

[52]W. Martienssen, "The optical absorption edge in ionic crystals," Phys. Chem. Solids **2**, 257 (1957).

[53]C. H. Grein and S. John, "Temperature dependence of the fundamental optical absorption edge in crystals and disordered semiconductors," Solid State Commun. **70**, 87 (1989).

[54]C. H. Grein and S. John, "Temperature dependence of the Urbach optical absorption edge: A theory of multiple phonon absorption and emission sidebands," Phys. Rev. B **39**, 1140 (1989).

[55]D. Malacara and B. J. Thompson, *Handbook of Optical Engineering* (CRC Press, 2001).

[56]P. Campbell and M. A. Green, "Light trapping properties of pyramidally textured surfaces," J. Appl. Phys. **62**, 243 (1987).

[57]J. Zhao, A. Wang, P. Campbell, and M. A. Green, "22.7% efficient silicon photovoltaic modules with textured front surface," IEEE Trans. Electron Devices **46**, 1495–1497 (1999).

[58]H. Y. Chen *et al.*, "Enhanced performance of solar cells with optimized surface recombination and efficient photon capturing via anisotropic-etching of black silicon," Appl. Phys. Lett. **104**, 193904 (2014).

[59]M. F. Abdullah, M. A. Alghoul, H. Naser, N. Asim, S. Ahmadi, B. Yatim, and K. Sopian, "Research and development efforts on texturization to reduce the optical losses at front surface of silicon solar cell," Renewable Sustainable Energy Rev. **66**, 380–398 (2016).

[60]N. Borojevic, A. Lennon, and S. Wenham, "Light trapping structures for silicon solar cells via inkjet printing," Phys. Status Solidi A **211**, 1617–1622 (2014).

[61]H. Y. Chen, H. L. Lu, Q. H. Ren, Y. Zhang, X. F. Yang, S. J. Ding, and D. W. Zhang, "Enhanced photovoltaic performance of inverted pyramid-based nanostructured black-silicon solar cells passivated by an atomic-layer deposited Al₂O₃ layer," Nanoscale **7**, 15142–15148 (2015).

[62]K. Chen, Y. Liu, X. Wang, L. Zhang, and X. Su, "Novel texturing process for diamond-wire-sawn single-crystalline silicon solar cell," Sol. Energy Mater. Sol. Cells **133**, 148–155 (2015).

[63]J. Eisenlohr, N. Tucher, O. Hohn, H. Hauser, M. Peters, P. Kiefel, J. C. Goldschmidt, and B. Blasi, "Matrix formalism for light propagation and absorption in thick textured optical sheets," Opt. Express **23**, A502–A518 (2015).

[64]N. Tucher, J. Eisenlohr, P. Kiefel, O. Hohn, H. Hauser, M. Peters, C. Müller, J. C. Goldschmidt, and B. Bläsi, "3D optical simulation formalism OPTOS for textured silicon solar cells," Opt. Express **23**, A1720–A1734 (2015).

[65]N. Tucher, J. Eisenlohr, H. Gebrewold, P. Kiefel, O. Hohn, H. Hauser, J. C. Goldschmidt, and B. Blasi, "Optical simulation of photovoltaic modules with multiple textured interfaces using the matrix-based formalism OPTOS," Opt. Express **24**, A1083–A1093 (2016).

[66]R. A. Street, P. Qi, R. Lujan, and W. S. Wong, "Reflectivity of disordered silicon nanowires," Appl. Phys. Lett. **93**, 163109 (2008).

[67]X. Liu, P. R. Coxon, M. Peters, B. Hoex, J. M. Cole, and D. J. Fray, "Black silicon: Fabrication methods, properties and solar energy applications," Energy Environ. Sci. **7**, 3223 (2014).

[68]M. Steglich, T. Kasebier, M. Zilk, T. Pertsch, E. Kley, and A. Tunnermann, "The structural and optical properties of black silicon by inductively coupled plasma reactive ion etching," J. Appl. Phys. **116**, 173503 (2014).

[69]M. Otto *et al.*, "Black silicon photovoltaics," Adv. Opt. Mater. **3**, 147–164 (2015).

[70]H. Savin, P. Repo, G. von Gastrow, P. Ortega, E. Calle, M. Garín, and R. Alcubilla, "Black silicon solar cells with interdigitated back-contacts achieve 22.1% efficiency," Nat. Nanotechnol. **10**, 624–628 (2015).

[71]See https://www.trinasolar.com/us/resources/blog/black-silicon-solar-modules-powerful-and-pleasing-design for more information about the efficiencies.

[72]S. John and R. Rangarajan, "Optimal structures for classical wave localization: An alternative to the Ioffe-Regel criterion," Phys. Rev. B **38**, 10101 (1988).

[73]B. M. Kayes, H. A. Atwater, and N. S. Lewis, "Comparison of the device physics principles of planar and radial *p-n* junction nanorod solar cells," J. Appl. Phys. **97**, 114302 (2005).

[74]Y. Huang, S. Chattopadhyay, Y. Jen, C. Peng, T. Liu, Y. Hsu, C. Pan, H. Lo, C. Hsu, Y. Chang, C. Lee, K. Chen, and L. Chen, "Improved broadband and quasi-omnidirectional anti-reflection properties with biomimetic silicon nanostructures," Nat. Nanotechnol. **2**, 770 (2007).

[75]J. Zhu, Z. Yu, G. F. Burkhard, C. Hsu, S. T. Connor, Y. Xu, Q. Wang, M. McGehee, S. Fan, and Y. Cui, "Optical absorption enhancement in amorphous silicon nanowire and nanocone arrays," Nano Lett. **9**, 279 (2009).

[76]L. Tsakalakos, J. E. Balch, J. Fronheiser, M. Shih, S. F. LeBoeuf, M. Pietrzykowski, P. J. Codella, B. A. Korevaar, O. Sulima, J. Rand, A. Davuluru, and U. D. Rapol, "Strong broadband optical absorption in silicon nanowire films," J. Nanophotonics **1**, 013552 (2007).

[77]K. X. Wang, Z. Yu, V. Liu, A. Raman, Y. Cuief, and S. Fan, "Light trapping in photonic crystals," Energy Environ. Sci. **7**, 2725–2738 (2014).

[78]L. Hu and G. Chen, "Analysis of optical absorption in silicon nanowire arrays for photovoltaic applications," Nano Lett. **7**, 3249–3252 (2007).

[79]Y. Lee, D. S. Ruby, D. W. Peters, B. B. McKenzie, and J. W. P. Hsu, "ZnO nanostructures as efficient antireflection layers in solar cells," Nano Lett. **8**, 1501–1505 (2008).

[80]Z. Yang, L. Ci, J. A. Bur, S. Y. Lin, and P. M. Ajayan, "Experimental observation of an extremely dark material made by a low-density nanotube array," Nano Lett. **8**, 446–451 (2008).

[81]O. L. Muskens, J. G. Rivas, R. E. Algra, E. P. A. M. Bakkers, and A. Lagendijk, "Design of light scattering in nanowire materials for photovoltaic applications," Nano Lett. **8**, 2638–2642 (2008).

[82]J. Gjessing, A. S. Sudbø, and E. S. Marstein, "Comparison of periodic light-trapping structures in thin crystalline silicon solar cells," J. Appl. Phys. **110**, 033104 (2011).

[83]H. Hsiao, H. Chang, and Y. Wu, "Design of anti-ring back reflectors for thin-film solar cells based on three-dimensional optical and electrical modeling," Appl. Phys. Lett. **105**, 061108 (2014).

[84]P. Chen *et al.*, "Periodic anti-ring back reflectors for hydrogenated amorphous silicon thin-film solar cells," Opt. Express **22**, A1128 (2014).

[85]K. Q. Le and S. John, "Synergistic plasmonic and photonic crystal light-trapping: Architectures for optical up-conversion in thin-film solar cells," Opt. Express **22**, A1 (2014).

[86]A. Taflove and S. C. Hagness, *Computational Electrodynamics: The Finite Difference Time-Domain Method* (Artech House, Boston, 2005).

[87]I. Valuev, A. Deinega, A. Knizhnik, and B. Potapkin, "Creating numerically efficient FDTD simulations using generic C++ programming," Lect. Notes Comput. Sci. **4707**, 213 (2007).

[88]S. Eyderman and S. John, "Light-trapping and recycling for extraordinary power conversion in ultra-thin gallium-arsenide solar cells," Sci. Rep. **6**, 28303 (2016).

[89]See http://fdtd.kintechlab.com/en/download for more information about the software.

[90]A. W. Blakers, "Shading losses of solar-cell metal grids," J. Appl. Phys. **71**, 5237 (1992).

[91]M. F. Schumann, S. Wiesendanger, J. C. Goldschmidt, B. Blasi, K. Bittkau, U. W. Paetzold, A. Sprafke, R. B. Wehrspohn, C. Rockstuhl, and M. Wegner, "Cloaked contact grids on solar cells by coordinate transformations: Designs and prototypes," Optica **2**, 850–853 (2015).

[92]M. Langenhorst, M. F. Schumann, R. Schmager, J. Lehr, U. Lemmer, M. Wegener, B. Richards, and U. W. Paetzold, "Performance of silicon solar cells with cloaked contact fingers under realistic conditions," in *Light, Energy and the Environment, OSA Technical Digest (online)* (OSA, 2017), p. PW2A.3.

[93]M. F. Schumann, M. Langenhorst, M. Smeets, K. Ding, U. W. Paetzold, and M. Wegener, "All-angle invisibility cloaking of contact fingers on solar cells by refractive free-form surfaces," Adv. Opt. Mater. **5**, 1700164 (2017).

[94]E. S. Roman, A. Vitrey, J. Buencuerpo, I. Prieto, J. M. Llorens, A. Garcia-Martin, B. Alen, A. Chaudhuri, A. Neumann, S. R. J. Brueck, and J. M. Ripalda, "Cloaking of solar cell contacts at the onset of Rayleigh scattering," Sci. Rep. **6**, 28669 (2016).

[95]E. V. Kerschaver and G. Beaucarne, "Back-contact solar cells: A review," Prog. Photovoltaics: Res. Appl. **14**, 107–123 (2005).

[96]C. Battaglia, A. Cuevas, and S. D. Wolf, "High-efficiency crystalline silicon solar cells: Status and perspectives," Energy Environ. Sci. **9**, 1552–1576 (2016).

[97]M. K. Mat Desa, S. Sapeai, A. W. Azhari, K. Sopian, M. Y. Sulaiman, N. Amin, and S. H. Zaidi, "Silicon back contact solar cell configuration: A pathway towards higher efficiency," Renewable Sustainable Energy Rev. **60**, 1516–1532 (2016).

[98] A. Deinega and S. John, "Effective optical response of silicon to sunlight in the finite-difference time-domain method," Opt. Lett. **37**, 112 (2012).

[99] J. Zhao and A. Wang, "Rear emitter *n*-type passivated emitter, rear totally diffused silicon solar cell structure," Appl. Phys. Lett. **88**, 242102 (2006).

[100] J. Benick, B. Steinhauser, R. Muller, J. Bartsch, M. Kamp, A. Mondon, A. Richter, M. Hermle, and S. Glunz, "High efficiency n-type PERT and PERL solar cells," in *Proceedings of the 40th Photovoltaic Specialist Conference (PVSC)* (IEEE, 2014), p. 3637.

[101] W. Cai, S. Yuan, Y. Sheng, W. Duan, Z. Wang, Y. Chen, Y. Yang, P. P. Altermatt, P. J. Verlinden, and Z. Feng, "22.2% efficiency n-type PERT solar cell," Energy Procedia **92**, 399 (2016).

[102] F. Kiefer, J. Krugener, F. Heinemeyer, M. Jestremski, H. J. Osten, R. Brendel, and R. Peibst, "Bifacial, fully screen-printed n-PERT solar cells with BF$_2$ and B implanted emitters," Sol. Energy Mater. Sol. Cells **157**, 326 (2016).

[103] F. Feldmann, M. Simon, M. Bivour, C. Reichel, and M. Hermle, "Efficient carrier-selective p- and n-contacts for Si solar cells," Sol. Energy Mater. Sol. Cells **131**, 100 (2014).

[104] F. Feldmann, M. Bivour, C. Reichel, M. Hermle, and S. W. Glunz, "Passivated rear contacts for high-efficiency *n*-type Si solar cells providing high interface passivation quality and excellent transport characteristics," Sol. Energy Mater. Sol. Cells **120**, 270 (2014).

[105] C. Schinke, P. C. Peest *et al.*, "Uncertainty analysis for the coefficient of band-to-band absorption of crystalline silicon," AIP Adv. **5**, 067168 (2015).

[106] See http://fdtd.kintechlab.com/en/fitting for more information about the fitting tool.

[107] Synopsys, Synopsys TCAD, M-Foundation Release 2016.12, 2016.

[108] K. A. Collett, R. S. Bonnilla, P. Hamer, G. Bourret-Sicotte, R. Lobo, T. Kho, and P. R. Wilshaw, "An enhanced alneal process to produce SRV < 1 cm/s in 1 Ω cm n-type Si," Sol. Energy Mater. Sol. Cells **173**, 50–58 (2017).

[109] R. S. Bonilla, B. Hoex, P. Hamer, and P. R. Wilshaw, "Dielectric surface passivation for silicon solar cells: A review," Phys. Status Solidi A **214**, 1700293 (2017).

[110] P. Mahtani, K. R. Leong, B. Jovet, D. Yeghikyan, and N. P. Kherani, "High quality amorphous–crystalline silicon heterostructure prepared by grid-biased remote radio-frequency plasma enhanced chemical vapor deposition," J. Non-Cryst. Solids **358**, 3396–3402 (2012).

[111] P. Mahtani, "High-quality amorphous-crystalline silicon heterostructures using the grid-based triode radio-frequency plasma enhanced chemical vapour deposition method," Ph.D. thesis, University of Toronto, 2014.

[112] A. Cuveas, "Surface recombination velocity of highly doped *n*-type silicon," J. Appl. Phys. **80**, 3370 (1996).

[113] S. J. Robinson, S. R. Wenham, P. P. Altermatt, A. G. Aberle, G. Heiser, and M. A. Green, "Recombination rate saturation mechanisms at oxidized surfaces of high-efficiency silicon solar cells," J. Appl. Phys. **78**, 4740–4754 (1995).

[114] A. G. Aberle, S. Glunz, and W. Warta, "Impact of illumination level and oxide parameters on Shockley-Read-Hall recombination at the Si-SiO$_2$ interface," J. Appl. Phys. **71**, 4422–4431 (1992).

[115] S. Foster and S. John, "Light-trapping design for thin-film silicon-perovskite tandem solar cells," J. Appl. Phys. **120**, 103103 (2016).